ZIP13 regulates lipid metabolism by changing intracellular iron and zinc balance

Ayako Fukunaka[1#]*, Gen Tanaka[2#], Toru Kimura[2,3#], Kowit Hengphasatporn[4], Daisuke Saito[1,5], Mayo Shigeta[6], Hiroshi Shibata[7], Takayuki Ichinose[8], Ichitaro Abe[9,10], Mari Shimura[11,12], Takashi Sato[1], Yuko Nakagawa[1], Takuro Horii[13], Izuho Hatada[13,14], Shingo Kajimura[10], Hiroshi Kiyonari[6], Hiroyuki Sakurai[2], Yasuteru Shigeta[4], Hirotaka Watada[5], Toshiyuki Fukada[15]*, and Yoshio Fujitani[1]*

[1] Laboratory of Developmental Biology & Metabolism, Institute for Molecular & Cellular Regulation, Gunma University, Maebashi, Gunma, Japan

[2] Department of Pharmacology and Toxicology, Kyorin University School of Medicine, Mitaka, Tokyo, Japan

[3] Laboratory of Biomedicinal Science, Department of Pharmaceutical Science, Faculty of Pharmacy and Pharmaceutical Science, Josai University, Saitama, Japan

[4] Center for Computational Sciences, University of Tsukuba, Tsukuba, Ibaraki, Japan

[5] Department of Metabolism & Endocrinology, Juntendo University Graduate School of Medicine, Tokyo, Japan

[6] Laboratory for Animal Resource and Genetic Engineering, RIKEN Center for Biosystems Dynamics Research, Hyogo, Japan

[7] Laboratory of Epigenetics and Metabolism, Institute for Molecular & Cellular Regulation,

21 Gunma University, Maebashi, Gunma, Japan

22 [8] Inorganic Analysis Laboratories, Toray Research Center, Inc., Shiga, Japan

23 [9] Department of Cardiology ad Clinical Examination, Oita University, Faculty of Medicine,

24 Oita, Japan

25 [10] Division of Endocrinology, Diabetes and Metabolism, Beth Israel Deaconess Medical Center

26 and Harvard Medical School, Boston, MA, USA

27 [11] Research Institute, National Center for Global Health and Medicine, Tokyo, Japan

28 [12] RIKEN SPring-8 Center, Hyogo, Japan

29 [13] Laboratory of Genome Science, Institute for Molecular & Cellular Regulation, Gunma

30 University, Maebashi, Gunma, Japan

31 [14] Viral Vector Core, Gunma University Initiative for Advanced Research (GIAR), Maebashi,

32 Gunma, Japan

33 [15] Faculty of Pharmaceutical Sciences, Tokushima Bunri University, Tokushima, Japan

34

35 ***Corresponding author**

36 E-mail: fukada@ph-bunri-u.ac.jp (T.F.), fukunaka@gunma-u.ac.jp (A.F.), and

37 fujitani@gunma-u.ac.jp (Y.F.)

38 [#] These authors contributed equally to this work.

39

40 ***Keywords:*** ZIP13, iron, lipolysis, adipocyte, lipid metabolism

41

42 ***Short title:*** ZIP13 regulates lipolysis by iron transport

43

44 ***Abbreviations:***

45 RER: respiratory exchange ratio, HFD: high-fat-diet, STD: standard diet, ER, endoplasmic
46 reticulum, PKA: protein kinase A, ICP-MS: inductively coupled plasma mass spectrometry,
47 EDSSPD3: Ehlers-Danlos syndrome spondylocheirodysplastic type 3, NEFA: nonesterified
48 fatty acid, MT: metallothionein, PDE: phosphodiesterase, 4F2hc: 4F2 cell-surface antigen
49 heavy chain, SVF: stromal vascular fraction, IRP2: iron regulatory protein 2, TfR: transferrin
50 receptor, Fth1: ferritin heavy chain, FTL: ferritin light chain, NAC: N-acetylcysteine, FACS:
51 fluorescence-activated cell sorting, WAT: white adipose tissue.

52

Abstract

Metabolic diseases are caused by a prolonged energy imbalance, and adipose tissue is known to be the main contributor. We previously reported that ZIP13, an Slc39a transporter whose deficiency causes Ehlers-Danlos syndrome spondylocheirodysplastic type 3 associated with lipoatrophy, inhibits the adipocyte browning pathway by modulating intracellular zinc status. The precise mechanisms of how ZIP13 regulates the homeostasis of adipose tissue remain unclear and therefore, we investigated the role of ZIP13 in mature adipocytes using adipocyte-specific *Zip13*-deficient mice. We herein demonstrate that these mice show accelerated lipolysis and reduced respiratory exchange ratio. In addition, abundance of iron and zinc balance were altered during differentiation in normal adipocytes, whereas iron distribution was substantially affected in *Zip13*-deficient adipocytes, which downregulated PDE activity and enhanced β-adrenergic receptor signaling pathways. Importantly, we confirmed that ZIP13 could transport both zinc and iron, using the *Xenopus* oocyte transport system and *in silico* structural dynamics simulations, and that the defect in iron distribution perturbs proper lipolysis. Together, these results illustrate that ZIP13 acts as a key regulator for lipolysis in adipocytes via the proper use of metals, and that the ZIP13-iron axis plays an important role in regulation of lipid metabolism. (193 word)

Introduction

Obesity and its associated metabolic diseases are caused by a long-term imbalance between energy intake and energy expenditure. Adipose tissue, which is a major factor in controlling the energy balance, is composed of white and brown adipocytes, which have two distinct functions; i.e., white adipocytes store excess energy, whereas brown adipocytes specialize in consuming energy [1, 2]. As chronic caloric excess is a main drivers of the development of obesity and type 2 diabetes, most studies have mainly focused on macronutrients, such as the effects of the types or compositions of fats and carbohydrates on metabolic diseases. However, little is known about the role of micronutrients and the proteins that regulate the homeostasis of each micronutrient in obesity and type 2 diabetes [3, 4, 5, 6, 7, 8]. Therefore, in this study, we aimed to investigate how essential trace elements are involved in metabolic homeostasis and events, by focusing on proteins associated with iron, zinc, and micronutrients, such metal ion transporters.

Zrt/Irt proteins (ZIPs and SLC39A) consist of a family of divalent metal ion transporters. Zrt stands for zinc-regulated transporter, which was named after identification of the yeast zinc importer, and Irt stands for iron-regulated transporter after the plant iron importer was discovered [9]. Although some ZIP members selectively transport zinc, as can be inferred from the name of ZIP, other members, such as ZIP8 and ZIP14, have broader substrate specificity and transport divalent metal ions, including zinc, iron, manganese, and cadmium *in vitro* [10, 11]. Genetic approaches involving gene-

knockout (KO) mice and human diseases indicate that the physiologically transported substrate of ZIP8 and ZIP14 *in vivo* is manganese ions [12, 13, 14]. ZIP13 is an intracellular ZIP member that has been reported to be localized to the Golgi, which was demonstrated to predominantly transport zinc ions by a competition assay using other metals, including iron [15]. We and other groups have also demonstrated that zinc levels are altered upon either ectopic expression or downregulation of ZIP13, all of which were analyzed using zinc-specific probes or by measuring metallothionein (*MT*) expression [15, 16, 17, 18], because ZIP13 localizes to the intracellular compartment which makes it difficult to elucidate whether ZIP13 can transport the zinc, or other metals, *in vivo* and *in vitro*.

Among the ZIP family members, ZIP8, ZIP14 and ZIP13 have been reported to participate in metabolic regulation, and hence their dysfunctions are associated with diseases, such as obesity, abnormal high density lipoprotein cholesterol levels, lipodystrophy, etc. [19, 20, 21]. We and other group previously demonstrated that ZIP13 plays an important role in the development of connective tissue in mice and humans, and its dysfunction causes Ehlers-Danlos syndrome spondylocheirodysplastic type 3(EDSSPD3, OMIM 612350), which is a very rare autosomal recessive disease in which patients develop lipoatrophy, strongly indicating the crucial role of ZIP13 in fat tissues homeostasis [21, 22]. We also reported that *Zip13* KO preferentially promotes beige adipocyte biogenesis and energy expenditure, thereby ameliorating diet-induced obesity and insulin resistance [18], although the precise molecular mechanisms by which ZIP13 controls adipocytes functions remain unclear.

Here, we investigated the role of ZIP13 in mature adipocytes, using adipocyte-specific *Zip13* KO (Adipo-*Zip13*KO) mice showed accelerated lipolysis in adipocytes leading to reduced respiratory exchange ratios (RER). We also found that abundance of iron and zinc balance was altered during differentiation in control adipocytes, whereas iron distribution was substantially affected in *Zip13*-deficient adipocytes, which downregulated PDE activity and enhanced β-adrenergic receptor signaling pathways. Furthermore, we confirmed that ZIP13 can transport both zinc and iron, using the *Xenopus* oocyte transport system and *in silico* structural dynamics simulations, and that ZIP13-mediated intracellular iron homeostasis is crucial for proper lipid metabolism. Together, these results indicate that ZIP13 regulates lipolysis in adipocytes via the proper use of metals, demonstrating the ZIP13-iron axis plays an important role in regulation of lipid metabolism.

Results

Adipo-*Zip13*KO mice demonstrate accelerated lipolysis in a cell-autonomous manner

To investigate the intrinsic role of ZIP13 in mature adipocytes, we generated adipocyte-specific *Zip13* KO mice by crossing *Zip13flox/flox;* adiponectin-Cre mice with *Zip13*+/- mice (hereafter referred to as Adipo-*Zip13*KO mice), in which we confirmed that *Zip13* mRNA expression was reduced in all fat tissues analyzed (Fig. 1A). Adipo-*Zip13*KO mice appeared to be resistant to an increase in body weight under HFD conditions (Fig. 1B and C), similar to systemic *Zip13* KO mice [18]. We also found that the body weights of Adipo-*Zip13*KO mice were decreased even in the standard diet (STD) condition in mice older than 30 weeks (Fig. 1D), together with a reduction in adipose tissues weight, particularly in subcutaneous fat tissue (Fig. 1E, and Figs. S1A and B). Intriguingly, Adipo-*Zip13*KO mice appeared to have normal glucose tolerance, but their insulin concentrations were lower than those of Ctrl mice under STD condition (Fig. S1C and D). Consistent with these results, insulin sensitivity of Adipo-*Zip13*KO mice under HFD conditions was improved compared with that of Ctrl mice (Fig. S1E). Taken together, Adipo-*Zip13*KO mice appeared less susceptible to HFD induced insulin resistance.

To elucidate the mechanism of this phenotype observed in Adipo-*Zip13*KO mice, we investigated the metabolic state of the mice. Energy expenditure (Fig. S2A and B), food intake (Fig. S2C), locomotor activity (Fig. S2D), and rectal temperature (Fig. S2E) were comparable between Adipo-*Zip13*KO mice and Ctrl mice in STD condition. Gene expression analysis showed that modest

141 but not statistically significant increases of *Ucp1* and *Cidea* expression are observed in the
142 subcutaneous fat tissue of Adipo-*Zip13*KO mice (Fig. S2F). A similar gene expression pattern was
143 observed in differentiated cells from subcutaneous fat tissue of Adipo-*Zip13*KO mice and these
144 changes were also observed under the treatment with β-adrenergic receptor agonist isoproterenol (Fig.
145 S2G). In addition, histology data showed the cell size of brown and white adipocytes is smaller in
146 Adipo-*Zip13*KO mice under STD condition (Fig. S2H). We also measured the whole-body oxygen
147 consumption (VO2) of Adipo-*Zip13*KO mice under different environmental temperatures. We found
148 that their VO2 levels showed tendency to be increased (Fig. S2I), although the expression of brown
149 fat markers was comparable (Fig. S2J). These results suggest that a modest increase in whole-body
150 oxygen consumption may cause the resistance to high-fat diet-induced obesity and insulin resistance.

151 Moreover, we found that RER was decreased in Adipo-*Zip13*KO mice (Fig. 1F and G: 20-
152 week-old mice; Fig. S3A and B: 30-week-old mice in STD condition), suggesting that Adipo-*Zip13*-
153 KO mice preferentially use lipids as an energy source rather than carbohydrates. We next investigated
154 why Adipo-*Zip13*KO mice had decreased RER, then hypothesized that *Zip13*-deficient mature
155 adipocytes might have accelerated lipolysis. To assess the degree of lipolysis, we measured
156 circulating nonesterified fatty acid (NEFA) levels in the plasma of Adipo-*Zip13*KO mice in response
157 to β-adrenergic stimulation, and found that their release of NEFA into the plasm was upregulated
158 upon the administration of the isoproterenol, in the fasting condition (Fig. 1H), which suggests that
159 the sympathetic nerve stimulated lipolysis was enhanced in Adipo-*Zip13*KO mice. We also found that

subcutaneous fat tissue is the predominant fat tissue responsible for increased release of NEFA in Adipo-*Zip13*KO mice (Fig. 1I). We further investigated whether this accelerated lipolysis occurs in a cell-autonomous manner. We first isolated preadipocytes from the subcutaneous fat tissue of each mouse, and differentiated them into white adipocytes, followed by measurement of NEFA release into the medium. Unexpectedly, we found that NEFA release was increased in adipocytes of *Zip13*-deficient mice, upon isoproterenol stimulation in a cell-autonomous manner (Fig. 1J). Expression patterns of genes associated with lipolysis and lipid metabolism in the subcutaneous fat tissues of Adipo-*Zip13*KO mice were comparable with those of Ctrl mice (Fig. S3C). These results indicated that in Adipo-*Zip13*KO mice, lipolysis was accelerated in a cell-autonomous manner, even independent of the insulin level, without apparent changes in the expression levels of genes associated with the lipolysis process.

Upregulation of cellular iron levels in mature adipocytes from Adipo-*Zip13*KO mice

We next aimed to investigate how ZIP13 is involved in the inhibition of lipolytic activity. It has been reported that mammalian ZIP13 transports zinc, whereas *Drosophil*a ZIP13 (dZIP13) transports iron [23], and therefore we assessed the cellular level of each metal using inductively coupled plasma mass spectrometry (ICP-MS) analysis and chemical probes (FluoZin-3 and FerroOrange for zinc ion (Zn^{2+}) and the ferrous iron ion (Fe^{2+}), respectively). Although zinc and iron levels in whole cells were not different between Ctrl and Adipo-*Zip13*KO mature adipocytes (Fig. 2A), organelle-

179 associated Fe^{2+} levels, but not Zn^{2+} levels, were decreased in mature *Zip13* KO adipocytes (Fig. 2B).
180 Based on reports that FerroOrange can label mainly endoplasmic reticulum (ER) and Golgi Fe^{2+} [24]
181 and ZIP13 localized in both Golgi and ER (Fig. 2C), this result suggested that Fe^{2+} levels are
182 decreased mainly in ER of mature *Zip13* KO adipocytes. We also analyzed the protein expression of
183 iron regulatory protein 2 (IRP2), transferrin receptor (TfR), ferritin heavy chain (Fth1), and ferritin
184 light chain (FTL), as the expression of these proteins is associated with iron metabolism. We found
185 that the expression of both IRP2 and TfR was decreased by stimulation with isoproterenol, whereas
186 the expression of Fth1 and FTL tended to be increased, although the Fth1 expression is not
187 significantly (Fig. 2D and E). These results indicate that Fe^{2+} levels are increased in the cytosol of
188 *Zip13* KO mature adipocytes, whereas they are decreased within their organelle including ER.
189

190 **ZIP13-mediated iron negatively regulates lipolytic activity**

191 Next, we assessed whether the ectopic expression of ZIP13 could increase the Fe^{2+} levels of
192 organelles. Either the wild-type form of mouse ZIP13 (ZIP13-WT) or its H254A mutant (ZIP13-
193 H254A), in which metal transport activity is attenuated [18, 25], was retrovirally expressed in *Zip13* KO
194 preadipocytes, followed by their differentiation into mature adipocytes. The cells were then harvested
195 on the second day (referred to as preadipocytes) or the sixth day (referred to as mature adipocytes)
196 (Fig. 3A). In the preadipocytes, we observed that the expression of ZIP13-WT induced an increase in
197 cellular Zn^{2+} but not Fe^{2+} levels in organelles, and this change was reduced in the expression of ZIP13-

198 H254A compared to ZIP13-WT expression (Fig. 3B). Intriguingly, in mature adipocytes, not only
199 cellular Zn^{2+} but also Fe^{2+} levels in organelles were increased by ZIP13-WT, although only Fe^{2+} levels
200 in organelles were reduced by the expression of ZIP13-H254A compared to ZIP13-WT expression
201 (Fig. 3C). These results suggest that ZIP13 may be involved in cellular zinc and iron homeostasis in
202 different ways depending on the adipocyte stage.

203 We next aimed to determine whether ZIP13-mediated metal transport is involved in the
204 lipolysis of mature adipocytes, using the mutant ZIP13-H254A, which impaired Fe^{2+} transporting
205 ability in mature adipocytes (Fig. 3C). We found that ZIP13-H254A could not suppress NEFA release
206 like ZIP13-WT does (Fig. 3D), suggesting that the Fe^{2+} transport ability of ZIP13 in the mature
207 adipocyte is required for the inhibition of lipolysis. Notably, ICP-MS analysis indicated that amounts
208 of iron were significantly increased in mature adipocytes, whereas their zinc levels were comparable
209 or rather tended to be lower than that of preadipocytes (Fig. 3E and F). These results suggest that
210 ZIP13 can transport both Zn^{2+} and Fe^{2+}, and that ZIP13-mediated Fe^{2+} plays a crucial role in
211 negatively regulating lipolysis in mature adipocytes. This result was reminiscent of a previous study
212 showing that iron-mediated lipolysis is caused by a pro-oxidant mechanism, in which
213 supplementation of the anti-oxidant N-acetyl cysteine (NAC) was shown to cancel iron-induced
214 NEFA release [26]. Therefore, we tested whether NAC treatment can reduce lipolysis in *Zip13*-deficient
215 mature adipocytes, and NAC treatment significantly inhibits NEFA release in mature adipocytes (Fig.
216 3G). Furthermore, hydroxy-radicals produced by Fe^{2+} mediated the Fenton reaction was increased in

217 Adipo-*Zip13*KO cells (Fig. S4), indicating that ZIP13-mediated Fe^{2+} sequestration in ER may be
218 involved in the degree of lipolysis, and dysfunction of ZIP13 increases cytoplasmic Fe^{2+} and pro-
219 oxidants levels, leading to NEFA release.

220

221 **Phosphodiesterase (PDE) activity is reduced in Adipo-*Zip13*KO cells**

222 How does ZIP13-mediated Fe^{2+} transport affect the lipolysis process? To address this question,
223 we focused on the β-adrenergic signaling pathway, which activates the lipolysis process in a cyclic
224 AMP (cAMP) and protein kinase A (PKA) -dependent manner [27]. We found that both levels of cAMP
225 and phosphorylated PKA (pPKA) were increased in *Zip13* KO mature adipocytes (Fig. 4A and B, Fig.
226 S5), suggesting that the steps upstream of cAMP are activated in these cells. On the other hand, NEFA
227 release from *Zip13*KO mature adipocytes was increased even upon treatment with forskolin, an
228 activator of adenylate cyclase (Fig. 4C), suggesting that the steps downstream of adenylate cyclase
229 would be affected in *Zip13* KO mature adipocytes. Then, we assessed the activity of PDE, which
230 degrades cAMP, and found that its activity was decreased in *Zip13* KO mature adipocytes (Fig. 4D),
231 suggesting that the decrease in the PDE activity would be responsible for the acceleration of lipolysis
232 by the loss of ZIP13. To confirm this point, we focused on PDE3 and PDE4, which are both
233 predominantly expressed in adipose tissues [28], and treated the cells with each inhibitor to see which
234 PDE predominantly plays a role in lipolysis. We found that the inhibition of PDE3 increased NEFA
235 release from Ctrl mature adipocytes but not from *Zip13* KO mature adipocytes (Fig. 4E), and such

236 increased NEFA release was not observed using a PDE4 inhibitor, suggesting that perturbation of
237 PDE3 may occur in *Zip13*-deficient mature adipocytes, which might be the main reason for the
238 increased cAMP level leading to the acceleration of lipolysis.

239 As *Zip13*-deficient mature adipocytes have increased Fe^{2+} in the cytosol, and pro-oxidants are
240 involved in facilitating lipolysis [26], we next investigated whether oxidative stress affects PDE activity.
241 We demonstrated that PDE activity was decreased by H_2O_2 treatment (Fig. 4F), which was consistent
242 with a previous report [29]. These results suggest that *Zip13*-deficient mature adipocytes have increased
243 Fe^{2+} in the cytosol and increased pro-oxidants, leading to the inhibition of PDE3, which results in the
244 enhancement of NEFA release.

245

246 **Mammalian ZIP13 transports both iron and zinc ions**

247 Crucial questions to be clarified were how *Zip13* deficiency caused the changes in the
248 subcellular distribution of Fe^{2+} level in mature adipocytes, and whether or not mammalian ZIP13
249 could transport iron directly, as ZIP13 has been recognized as a zinc-specific transporter that regulates
250 intracellular zinc homeostasis [15,16, 17, 18]. Although some ZIP family members, such as ZIP8 and ZIP14,
251 transport multiple metal ions, including zinc and iron [10], direct evidence of the transportation of Fe^{2+}
252 by mammalian ZIP13 has not been reported to date. To address these questions, we heterologously
253 expressed ZIP13 on the plasma membrane of *Xenopus* oocyte and examined its transport activity of
254 zinc and iron ions.. Upon injection of complementary RNA (cRNA) of the full-length form of mouse

255 ZIP13 (mZIP13), its protein was mainly expressed in intracellular spaces but not on the cell surface
256 of oocytes (Fig. 5A, upper left). This is the issue that has made it difficult to experimentally determine
257 substrates of ZIP13 that is transported, as ZIP13 is an intracellular transporter that localizes to the
258 ER/Golgi in mammalian cells. To circumvent this problem, we fused mZIP13 with human
259 SLC3A24/4F2 cell-surface antigen heavy chain (4F2hc), which is the subunit of this large neutral
260 amino acid transporters such as LAT1, to force the ZIP13 protein to be localized on the plasma
261 membrane (Fig. 5B). We confirmed that this fusion protein named 4F2hc-mZIP13-HA (4F2hc-m13)
262 was successfully and predominantly expressed on the surface of oocytes (Fig. 5A, lower left), which
263 was also true for the case of another fusion protein, 4F2hc-mZIP14-HA (4F2hc-m14), which was
264 used as a control (Fig. 5A, lower right). Three-dimensional structure simulation using Alphafold2
265 suggested that the structure of the metal transporting regions of these proteins might be unaffected
266 (Fig. 5C), and both 4F2hc-m13 and 4F2hc-m14 induced the expression of metallothionein 1 gene
267 *(MT1)*, an indicator of intracellular zinc level [16, 17, 18] in HEK293 cells when each of them was
268 ectopically expressed (Fig. 5D), indicating that both fusion transporters can transport zinc into cells.
269 Then, we assessed if these fusion transporters expressed on the plasma membrane of *Xenopus oocytes*
270 are able to mobilize zinc and iron ions, using the *Xenopus* oocyte transport assay with radioisotopes,
271 and demonstrated that the ZIP14-based fusion transporter 4F2hc-m14 as well as the ZIP13-based
272 fusion transporter 4F2hc-m13 transported zinc and iron (Fig. 5E and F). These results clearly
273 demonstrated that mammalian ZIP13 has the ability to transport both zinc and iron ions.

274

275 ***In silico* structural dynamics simulations of transport mechanism of mammalian ZIP13**

276 Lastly, we performed an *in silico* ion binding prediction in terms of static and dynamic
277 analyses using the ZincBind web server and molecular dynamics (MD) simulation, respectively. The
278 result predicted that Zn^{2+} could bind to M1 and M2 sites, which is relevant to N120, D225, N226,
279 H229, H254, E255, and E259 (Fig. 6A), similar to what was previously reported in ZIP8 [30]. The ion
280 binding stability of Zn^{2+} and Fe^{2+} was further evaluated using 0.5 μs-MD simulations for the wild-
281 type form of mouse ZIP13 (ZIP13-WT), with 3 replications for each system, totaling 6 systems. The
282 results showed a consistent trend across all replications of each system. However, it was observed
283 that only in #3, Zn^{2+} was trapped by H124 at the M1 site over the simulation time. For the
284 representative systems, this ion-binding analysis shows that both Zn^{2+} and Fe^{2+} at the M2 site could
285 stably bind to ZIP13-WT/Zn^{2+} and ZIP13-WT/Fe^{2+} after 0.33 μs (Fig. 6A and B). In contrast, ions at
286 the M1 site slightly fluctuated and subsequently moved out of this ion channel, particularly moving
287 out faster in the ZIP13-WT/Fe^{2+} compared to the ZIP13-WT/Zn^{2+} (Fig. 6A and B). Notably, Zn^{2+} at
288 the M1 site in ZIP13-WT stably bound until 0.17 μs, while the ion at M1 site of ZIP13-WT/Fe^{2+}
289 system rapidly moved out around 0.05 μs in all replications (Fig. 6B). Based on three replicates of
290 each system, we found that in one of the ZIP13-WT/Zn^{2+} simulations (run #3), Zn^{2+} at M1 remained
291 bound throughout the simulation time. This might indicate the superiority in Fe^{2+} transport kinetics.
292 Among amino acid residues in the M1 and M2 sites, E255 and E259 show a strong binding interaction

293 with both ions according to the occupancy of the ion at each residue (Fig. 6C). When the ion is
294 released from the M1 site, conformational changes in the side chain of H254 facilitate ion ejection,
295 confirming the important role of H254 in the ion transport of ZIP13. In this process, H254 binds Zn^{2+}
296 slightly longer than Fe^{2+}, which is probably the reason why Fe^{2+} is ejected faster from the ion binding
297 sites. These simulation results also support our experimental results that ZIP13 may serve a role in
298 transporting both Zn^{2+} and Fe^{2+} ions.

299 **Discussion**

300 Dysregulation of iron homeostasis is associated with several disease statuses including
301 diabetes and obesity [31]. For instance, high ferritin levels are positively correlated with central
302 adiposity [32], and iron deficiency is also associated with obesity [33, 34]. It has been reported that iron
303 regulates adipocyte function and homeostasis associated with adipogenesis and lipid metabolism. It
304 is widely known that iron is crucial for the generation of lipid peroxidation products, which are linked
305 with many pathophysiological statuses, and it is also true that iron overload under the condition of
306 obesity increases lipolysis and lipid peroxidation [26]. Although the role of iron in lipid metabolism has
307 been well-recognized, the molecular mechanism of how iron regulates lipid metabolism in adipose
308 tissues *in vivo* and its physiological significance is still poorly understood.

309 As we previously found that ZIP13 participates in adipose tissue homeostasis by regulating
310 the adipocyte browning [18], we herein investigated how ZIP13 is involved in maturing adipocyte
311 functions. We found that total iron and zinc levels in cells were comparable between control and
312 *Zip13* KO mature adipocytes (Fig. 2A), however, Fe^{2+} levels in the cytosol of *Zip13* KO mature
313 adipocytes were significantly increased (Fig. 2D and E) and correlated with the promotion of lipolysis
314 (Fig. 3). We also found that the cAMP/PKA signaling pathway was upregulated in *Zip13* KO mature
315 adipocytes, which was owing to the downregulation of PDE activity (most likely of PDE3, Fig. 4E).
316 This inhibition of PDE activity is due to increased reactive oxygen species (ROS), as the ROS
317 scavenger NAC moderates NEFA release. These results indicate that enhancement of the intracellular

318 iron-ROS axis in the absence of ZIP13 attenuates PDE activity in mature adipocytes, leading to an
319 increase in cAMP level and lipolysis (Fig. 7). To our knowledge, it was the first to demonstrate that
320 mammalian ZIP13 affects subcellular iron distribution without changing total cellular iron levels.
321 Although, the gross phenotypes of *Zip13* KO mice are reminiscent of those of the zinc-deficient
322 model suffering short stature and skin abnormalities, which are different from the phenotypes of iron
323 deficiency. On the other hand, it is also known that all the phenotypes or symptoms of *Zip13* KO or
324 EDSSPD3 patients cannot be explained solely by zinc dysregulation. Therefore, the ZIP13 mediated
325 intracellular transport of iron may be a novel mechanism that contributes to the lipolysis in mature
326 adipocytes *in vitro* and *in vivo*.

327 EDSSPD3 patients were found to have lipoatrophy and decreased adipose tissue mass, which
328 are closely associated with the phenotypes observed in Adipo-*Zip13*KO mice. A recent study showed
329 that there is an adipogenic progenitor cell population that expresses *Acta2* (encoding smooth muscle
330 actin (αSMA), and *Sm22*, *Pax3*, *Pdgfrα,* and *Cd81* were identified in the stromal vascular fraction
331 (SVF) of white adipose tissue (WAT) as precursors of beige adipocyte following cold exposure [35, 36,
332 37, 38]. Furthermore, WAT lipolysis-derived linoleic acid triggers beige progenitor cell proliferation
333 following cold acclimation, and β3-adorenoceptor activation [39]. As the expression of *Zip13* was also
334 observed in the SVF in addition to the adipocyte fraction (Fig. S6A), and CD81-positive proliferating
335 cells were increased in the SVF of *Zip13* KO mice (Fig. S6B), there are possibilities that ZIP13-
336 mediated lipolysis in mature adipocyte might be involved in the proliferation of beige progenitor cell

337 or that ZIP13 might be directly involved in the regulation of beige progenitor cells. Further analysis
338 is needed to elucidate the role of ZIP13 in beige progenitor cells and/or beige fat biogenesis.

339 We previously demonstrated that ZIP13-mediated zinc is necessary for the inhibition of beige
340 adipogenesis [18]. In the present study, we found that ZIP13 has the ability to transport both Fe^{2+} and
341 Zn^{2+}. Furthermore, we also found that H254 residue of ZIP13 is important for the transport Fe^{2+} and
342 Zn^{2+} by using both cell experiments (Fig. 3B and C) and *in silico* structural dynamics simulations
343 (Fig. 6), and that ZIP13-mediated iron distribution in mature adipocytes is important for proper
344 lipolytic function (Fig. 3D). Although it is well recognized that iron is an important metal affecting
345 many biological functions, its significance in subcellular distribution has remained poorly
346 characterized to date. Our results demonstrated that iron balance between cytosol and intracellular
347 vesicles such as ER and Golgi achieved through ZIP13 affect the degree of lipolysis induced by β-
348 adrenergic stimulation in the mature adipocyte. It is still unknown whether ZIP13 is the only molecule
349 that affect intracellular sequestration of iron ion, these results points to future investigation into the
350 elucidation of regulatory mechanism of intracellular iron distribution.

351 It is also an intriguing finding that ZIP13 may act as a dual-specificity transporter of Zn^{2+} and
352 Fe^{2+} during the maturation of adipocytes. In a metal ion transport assay using *E.coli*., dZIP13 was
353 found to transport only Fe^{2+}, unlike mammalian ZIP13 [23]. Furthermore, in contrast to mammalian
354 ZIP13, dZIP13 has potential iron-binding residues at both its N- and C-termini [40, 41]. This is consistent
355 with the fact that dZIP13 responds to iron and plays a specific role in iron homeostasis. In contrast,

356 mZIP13 regulates only zinc levels in preadipocyte cells, whereas mZIP13 regulates both iron and
357 zinc levels in mature adipocytes in our adipocyte differentiation system (Fig. 2 and Fig. 3), suggesting
358 that mZIP13 transports both Fe^{2+} and Zn^{2+} within cells in a context-dependent manner. The question
359 then arises as to how the specificity of substrate transport is determined in cells and tissues. One
360 possible factor that determines substrate specificity may be changes in intracellular and extracellular
361 environment. Notably, several studies reported that iron levels are increased during adipocyte
362 differentiation [42, 43]. Based on our (Fig. 3E and F) and other observations [42, 43], it is possible that
363 mZIP13 switches the main physiological substrate from Zn^{2+} to Fe^{2+} during adipocyte differentiation,
364 possibly responding to an increase in intracellular iron concentrations. To investigate our hypothesis,
365 we performed *in silico* structural dynamics simulation based on actual zinc and iron levels measured
366 by ICP-MS, and found that mZIP13 may preferentially transport Fe^{2+} over Zn^{2+} (Fig. 6). Further
367 analyses are needed to clarify the signals or timing that is important for "possible switching from zinc
368 to iron transport" by ZIP13.

369 Of particular importance in this study is the establishment of a transport assay system for ZIP
370 family existing on the membrane of intracellular compartment, such as ER or Golgi. Using 4F2hc
371 fusion ZIP transporters, we successfully expressed ZIP fusion proteins on the plasma membrane of
372 *Xenopus oocytes* and examine zinc and iron ion transport in the system (Fig. 5). Recent advances in
373 cryo-electron microscopy showed that, BbZIP, a ZIP homolog in *Bordetella bronchiseptica*,
374 transports Zn^{2+} in an elevator-type mechanism [44, 45, 46]; however, the molecular mechanism of ion

375 transport by ZIPs has not yet been clarified, although Zn^{2+}/HCO^{3-} and Zn^{2+}/H^{+} symport or water-
376 mediated transport mechanisms have been proposed [47, 48]. We believe that clarification of detailed
377 transport mechanisms of zinc and iron ions by ZIPs is the important next step in the field, for which
378 the established transport assay system in this study will contribute in creating a venue that highlights
379 and explores the various facets of ZIP family members.

380 In conclusion, our findings illustrate that ZIP13 acts as a key regulator for lipolysis in
381 adipocytes via the proper use of metals, and a picture is now emerging of the ZIP13-iron axis plays
382 an important role in regulation of lipid metabolism. With this realization that ZIP13 is a critical
383 regulator of intracellular metal homeostasis and lipid metabolism, it may become a focus of attention
384 for its potential to identify novel targets for therapeutic intervention in human disease.

385

386 **Methods**

387 **Animal studies**

388 All mice were housed in specific pathogen-free barrier facilities, maintained under a 12-h light/dark
389 cycle, given water *ad libitum*, and fed standard rodent food (Oriental Yeast, Tokyo, Japan) or rodent
390 food containing 60% fat (Research Diet, New Brunswick, NJ, USA) from 6 to 18 weeks of age [49].
391 *Zip13*-flox mice (Accession No. CDB1360K: https://large.riken.jp/distribution/mutant-list.html)
392 were generated by using TT2 embryonic stem cells derived from a hybrid strain between C57BL/6
393 and CBA [50]. To construct a targeting vector, genomic fragments of the *Zip13* locus were obtained
394 from a C57BL/6 BAC clone (BACPAC Resources). A 3.8 kbp region containing from exon 5 to 10
395 of the *Zip13* gene was flanked by loxP sites (Fig. S7). The targeted ES clones were microinjected into
396 8-cell stage ICR embryos, and the injected embryos were transferred into pseudopregnant ICR
397 females. The resulting chimeras were crossed with B6;SJL-Tg(ACTFLPe)9205Dym/J mice to
398 remove the drug-resistant Neo and Puro cassettes, and heterozygous offspring were identified by PCR
399 using the following primers: P1 (5'-CCA GCC AGGT GAG CCC CAA G-3') and P2 (5'-TTC CGG
400 GCA GAG GGC ACA GT-3') (WT; 1449 bp, Flox; 1730 bp), and P3 (5'-
401 ACCGGCTGCCTCTTCCACAT-3') and P4 (5'-GTG CCC CCT GCT GTG TGA GG-3') (WT; 513
402 bp, Flox; 689 bp). Adiponectin-Cre mice were obtained from Jackson Laboratories (strain no.
403 010803), and all mice were backcrossed onto C57BL/6J mice for more than seven generations.
404 Adipocyte-specific *Zip13* KO mice were generated by crossing *Zip13*-flox mice with adiponectin-

405 Cre mice. *Zip13f/f;* adiponectin-Cre mice were initially used as adipocyte-specific *Zip13* KO mice,
406 however, as they showed no obvious phenotypes associated with mature adipocytes such as RER and
407 VO2 values as observed in systemic *Zip13*KO mice, then we used *Zip13f/*(−)*;*adiponectin-Cre mice
408 were generated and used, because of their higher efficiency of KO compared with *Zip13f/f;*
409 adiponectin-Cre mice. In this study, we used *Zip13f/*(−); adiponectin-Cre mice were used as Adipo-
410 *Zip13*KO mice, and *Zip13f/*(+); adiponectin-Cre mice were used as Ctrl mice.

411

412 **Metabolic studies**

413 **Indirect calorimetry**

414 VO2 and VCO2 were measured in individual mice at the indicated ages using an Oxymax apparatus
415 (Columbus Instruments, Columbus, OH, USA). O_2 and CO_2 measurements were performed every 18
416 min over a 3-day period, during both the light and dark phases, and the data from the final day were
417 analyzed. Locomotor activity was measured in a metabolic chamber using an infrared light beam
418 detection system (ACTIMO-100; Shinfactory, Fukuoka, Japan). Total locomotor activity during a 12-
419 h period was measured.

420

421 **Cell immortalization and culture**

422 White preadipocytes were isolated from the subcutaneous fat tissue of Ctrl and Adipo-*Zip13*KO mice
423 (6 -8 weeks) by collagenase digestion, and then immortalized, as described previously [18]. Briefly,

424 preadipocytes were immortalized by retroviral transduction with the SV40 largeT antigens, and
425 selection with puromycin (2 mg/mL). Immortalized preadipocytes were a mixed population, and two
426 cell lines were analyzed. Preadipocytes were seeded onto collagen-coated dishes (Corning,
427 Kennebunk, ME, USA) in Dulbecco's Modified Eagle Medium (DMEM)/F12 (Gibco, Carlsbad, CA,
428 USA) with 10% fetal bovine serum (FBS). For white adipocyte differentiation, cells were induced
429 with induction medium containing 10% FBS, 5 μg/mL insulin (Humalin R, Eli Lilly), 250 μM
430 isobutylmethylxanthine (Sigma-Aldrich, St. Louis, MO, USA), 125 μM Indomethacin (Sigma), and
431 2 μg/mL dexamethasone (Sigma) in DMEM/F12 according to the manufacturer's protocol [51]. Two
432 days after induction, the culture medium was changed to a maintenance medium containing 10% FBS
433 and 5 μg/mL insulin. For isoproterenol treatment, cells were incubated with 10 μM isoproterenol for
434 2 h.

435

436 **Immunoblotting experiments**

437 Immunoblotting was performed as described previously [18, 52, 53, 54]. The following antibodies were
438 used for immunoblotting: anti-Fth1 (1:1,000; Abcam, St. Charles, MO, #EPR3004Y), anti-FTL
439 (1:1,000; Abcam, #ab69090), anti-IRP2 (1:1,000; Millipore, Bedford, MA, USA, #MABS2030), anti-
440 TfR (1:1000; Invitrogen, Carlsbad, CA, USA, #136890), anti-actin (1:5000, Sigma, #A2228), anti-
441 pPKA (1:1000; Cell Signaling, Danvers, MA #5661), PKA (1:1000; Cell Signaling, #5842) and anti-
442 GAPDH (1:3,000; Cell Signaling, #2118).

443

444 **Immunofluorescence experiment.**

445 *Xenopus laevis* oocytes injected with cRNAs were fixed with paraformaldehyde and embedded in
446 paraffin. The sliced sections were incubated with an anti-HA monoclonal antibody (1:1000;
447 BioLegend, San Diego, CA, USA, #901514), followed by anti-mouse Alex Fluor 488-conjugated
448 immunoglobulin (1:100; Thermo Fisher Scientific, Tokyo, Japan). The sections were mounted in
449 Fluorescence mounting medium (DAKO, Glostrup, Denmark). Fluorescence was visualized using an
450 Olympus Fluoview FV1000 laser confocal microscope. Images are the product of 3-fold line
451 averaging. Immunofluorescence experiment using preadipocytes were described previously [18, 52, 53].
452 The following antibodies were used: anti-GM130 (1:250; Transduction Lab, Lexington, KY, USA,
453 #610823), anti-Calreticulin (1:250; Thermo Fisher Scientific, #PA3-900), anti-HA (1:250; BioLegend,
454 San Diego, CA, USA, #901513) or anti-HA (1:100; MBL, Tokyo, Japan, #561).

455

456 **Gene expression analysis**

457 Total RNA was isolated from tissues using QIAzol (Qiagen, Valencia, CA, USA) following the
458 manufacturer's protocol. Reverse transcription reactions were performed using High Capacity cDNA
459 Synthesis Kit (Applied Biosystems, Foster, CA, USA). The sequences of the primers used in this
460 study are shown in Table S1. Quantitative reverse transcriptase Polymerase Chain Reaction (qRT-
461 PCR) was performed with SYBR green-fluorescent dye using an ABI 7500 Fast Real-Time PCR

462 System. Relative mRNA expression was determined by relative standard curve methods using *18S*
463 (for mouse), or *Gapdh* (for human) as an internal control to normalize samples.
464

465 **Plasmid construction and virus production**

466 C-terminally HA-tagged plasmids expressing mouse ZIP13 (mZIP13-HA) were described previously
467 [18]. Phoenix packaging cells were transfected using retroviral vectors by lipofection. After 48 h, the
468 viral supernatant was collected and filtered. Preadipocytes were incubated for 6 h with viral
469 supernatant supplemented with 10 μg/mL polybrene. For the construction of 4F2hc-m13 and 4F2hc-
470 m14, 4F2hc and mZIP13 or mZIP14 were fused by PCR and In-Fusion® HD Cloning Kit (Takara
471 Bio, Shiga, Japan), according to the manufacturer's instructions. In-Fusion PCR primers were
472 designed to share 15 bases of homology with the PCR fragments and vector ends. 4F2hc, ZIP13 and
473 ZIP14 plasmids, which had already been constructed previously [18, 55, 56], were used for PCR templates.
474 The PCR fragments were subcloned into the mammalian expression vector pcDNA 3.1(-) at an EcoRV
475 site.
476

477 ***In vivo* and *ex vivo* lipolysis.**

478 To determine *in vivo* lipolysis, circulating plasma NEFA levels were measured after overnight fasting
479 (12 h). Mice were then given an intraperitoneal (i.p.) injection of 10mg/kg for isoproterenol. Plasma
480 NEFAs were measured 30 min after injection. To determine *ex vivo* lipolysis, the release of NEFA

481 from adipose tissue was measured, as previously described [57]. Briefly, mice were sacrificed, and each
482 type of adipose tissue was excised. The fat pads were washed in prewarmed 2% bovine serum albumin
483 (BSA, Free fatty acid free)-DMEM/F12 medium. Adipose tissue pieces (20 mg) were incubated in
484 200 μL 2% BSA-DMEM/F12 medium with 5μM Triacsin C (Sigma) in the presence or absence of
485 10 μM isoproterenol. The medium was removed and used to measure NEFA release (NEFA kit,
486 WAKO). For protein quantification, fat explants were first incubated in 1 mL extraction solution
487 (chloroform: methanol, 2:1) and incubated for 60 min at 37 °C under vigorous shaking. Then, the
488 tissue pieces were transferred to 500 μL lysis solution (0.3 N NaOH/0.1% sodium dodecyl sulfate
489 (SDS)) and incubated overnight at 55 °C under vigorous shaking. Protein content was determined
490 using pierce 660 nm protein assay reagent (Thermo Fisher Scientific), and BSA as the standard.

491

492 **Cellular lipolysis assay**

493 Preadipocytes were incubated with a differentiation induction cocktail, and differentiated for 8 days.
494 Lipolysis was assessed by measuring NEFA release in the culture medium. The NEFA assay was
495 performed according to the manufacturer's instructions [57]. Briefly, aliquots of cell culture medium
496 (4μL) were added to 80 μL reagent A, and incubated at 37 °C for 10 min. This was followed by the
497 addition of 160 μL reagent B, and the incubation for another 37 °C for 10 min, and then absorbance
498 was measured at 550 nm. NEFA releases was normalized to total protein content using pierce 660 nm
499 protein assay reagent. For inhibitor treatment, cells were incubated with 50 μM rolipram (WAKO) or

500 10 μM cilostamide (Cayman) for 2 h.

501

502 **cAMP analysis**

503 The cAMP enzyme immunoassay (Cayman) was performed according to the manufacture's protocol.
504 Briefly, preadipocytes were differentiated into mature adipocytes, and treated with 10 μM
505 isoproterenol, and then cells were washed twice with ice-cold phosphate-buffer saline (PBS), lysed
506 by the addition of 1 mL 0.1 M HCl, and centrifuged at 1,000 *g* for 10 min. The supernatant was diluted
507 in enzyme-linked immunosorbent assay (ELISA) buffer (sample dilution: x3) and cAMP levels were
508 measured by enzyme immunoassay according to the manufacturer's protocol. cAMP levels were
509 normalized to protein content, which was determined by assaying the supernatant using the pierce
510 660 nm protein assay reagent.

511

512 **PDE activity assay**

513 PDE activity was measured using the PDE activity assay kit according to the manufacturer's protocol
514 (Abcam). PDE activity was normalized to protein content, by assaying the cell lysates using pierce
515 660 nm protein assay reagent.

516

517 **Zn^{2+} and Fe^{2+} measurements**

518 Zn^{2+} levels were measured using FluoZin-3 (Invitrogen, #F24194) as described previously [16]. Cells

519 were plated onto 24-well plates, and washed with Hanks' Balanced Salt Solution (HBSS) buffer
520 (Sigma-Aldrich) 3 times. The cells were then incubated with 3 μM FluoZin-3 for 1 h, and washed
521 with HBSS buffer 3 times. Fluorescence was recorded at 495 nm excitation and 517 nm emission
522 using EnSpire multimode plate reader (Parkin Elmer). Fe^{2+} levels were measured using FerroOrange
523 (DOJINDO, Kumamoto, Japan, #F374) as described previously [58]. Briefly, the cells were incubated
524 with 2 μM FerroOrange for 1 h. Fluorescence was recorded at 543 nm excitation and 580 nm emission.
525 For protein determination, cells were lysed with 250 μL lysis solution (0.3N NaOH/0.1% SDS), and
526 incubated at room temperature under vigorous shaking. Protein content was determined using pierce
527 660 nm protein assay reagent and BSA as a standard.
528

529 **cRNA preparation**

530 The oocyte expression vectors were linearized with Hind III and *in-vitro* transcribed to cRNA using
531 the mMESSAGE mMACHINE T7 Transcription Kit (Thermo Fisher Scientific). Synthesized cRNAs
532 were then polyadenylated with the Poly(A) Tailing Kit (Thermo Fisher Scientific) and purified with
533 the MEGAclear Transcription Clean-Up Kit (Thermo Fisher Scientific), according to the
534 manufacture's protocols.
535

536 **Oocyte preparation and transporter expression**

537 The oocyte transport assay was performed as previously reported [59]. Briefly, adult female *Xenopus*

538 *laevis* (Watanabe Zoshoku, Japan) were anesthetized with 1.0 to 1.5 mg/mL tricaine (Tokyo Chemical
539 Industry, Japan) and pieces of the ovary were surgically removed. Oocytes were isolated from the
540 ovary and defolliculated with 1.0 to 1.5 mg/mL collagenase A (Roche) in OR2 buffer (82 mM NaCl,
541 2.5 mM KCl, 1 mM $MgCl_2$, 5 mM HEPES; pH 7.6) at room temperature for 1.5 to 2 h. Defolliculated
542 oocytes were washed more than 5 times with OR2 buffer, and then transferred to ND96 buffer (96
543 mM NaCl, 2 mM KCl, 1.8 mM $CaCl_2$, 1 mM $MgCl_2$, 5 mM HEPES; pH 7.5). Stage IV to VI oocytes
544 were selected and injected with 18.4 nL (18.4 ng) of purified cRNAs, or equal volumes of RNA-free
545 water using Nanoject II microinjector (Drummond Scientific), and incubated for 2 days at 18 °C in
546 ND96 buffer before their use in the uptake assay.

547

548 **Metal uptake assay**

549 Six to eight cRNA-injected oocytes were placed in a 96-well plate, and washed twice with ND96
550 buffer. Uptake assays were started by replacing the buffer with 120 μL of iron uptake solution (ND
551 96 buffer containing 100 μM $FeCl_2$, 1 - 5 μCi/mL $^{55}FeCl_3$, and 1 mM ascorbic acid) or zinc uptake
552 solution (ND96 containing 100 μM $ZnSO_4$ and 1 - 2 μCi/mL $^{65}ZnCl_2$), and incubated at 22 °C for 240
553 min. The iron uptake was stopped by replacing the uptake solution with ice-cold ND96 supplemented
554 with 1 mM ascorbic acid. The oocytes were then transferred to a 24-well plate and washed 5 times
555 with the same buffer, solubilized with 0.0625 N NaOH, and radioactivity was measured by liquid
556 scintillation counting. The zinc uptake was stopped by replacing the uptake solution with ice-cold

557 ND96 buffer supplemented with 5 mM EDTA. The oocyte was transferred to 24-well plate and
558 washed 5 times with the same buffer. The amount of zinc in the oocytes was visualized by a Phosphor
559 Imager (Typhoon FLA 9500; GE Healthcare), and quantified by ImageJ software. Each experiment
560 was performed twice on different days.

561

562 **Structure prediction.**

563 Protein structure prediction of 4F2hc-m13 was performed using locally installed version of ColabFold
564 v1.3.0 [60], which is the optimized implementation version of the AlphaFold2. Five models of 4F2hc-
565 m13 were generated using 3 recycles and refined with AMBER force field. The models were
566 visualized and superimposed with the model of mouse ZIP13 (PDB ID: Q8BZH0) deposited in
567 AlphaFold DB using Mol* Viewer (Fig. S8) [61]. The predicted models were ranked by their pLDDT
568 value (a per-residue confidence score), and the m13 domain of the top-scored model (rank 1) was
569 superimposed with the m13 domains of the other models (Fig. S9).

570

571 **ICP-MS**

572 Preadipocyte and mature adipocytes were harvested with methanol and evaporated with centrifugal
573 concentration [62]. Samples were digested with 0.5 mL of HNO_3 (Tamapure-AA-100, Tama Chemical
574 Co. Ltd., Kanagawa, Japan) at 180 °C for 20 min in an ETHOS 1 microwave oven (Milestone, Srl,
575 Sorisole, Italy) and then diluted with ultra-pure water (manufactured by PURELAB Option-R 7 and

576 PURELAB flex UV, Veolia Water Solution and Technologies, Paris, France) to a 5-mL volume.
577 Concentrations of Fe and Zn were determined using inductively coupled plasma-sector field mass
578 spectrometry ICP-SFMS (ELEMENT XR, Thermo Fisher Scientific Inc., Bremen, Germany). ^{56}Fe
579 and ^{66}Zn were measured using medium resolution mode (R = 4,000). The methanol blank samples
580 were prepared without cells and analyzed in the same manner. The amounts of Fe and Zn amounts
581 were corrected by subtracting the mean amounts of the blank samples.

582

583 **Ion binding site prediction and analysis**

584 The 3D structure of mouse ZIP13 (ZIP13-WT), obtained from the AlphaFold2 database (UniProt ID:
585 Q8BZH0) [63], served as the structure for ion binding prediction. Structural pairwise alignment between
586 ZIP8, sourced from a previous study [30,] and ZIP13, alongside the ZincBind web server [64], facilitated
587 the prediction and confirmation of two ion coordination sites denoted as M1 and M2. Subsequently,
588 homo Zn^{2+} ions were positioned within M1 and M2 in ZIP13-WT. This methodology was used for
589 the homo Fe^{2+} system preparation. The parameters of the modified 12-6-4 Lennard-Jones (m-12-6-4-
590 LJ) non-bonded model for Zn^{2+} and Fe^{2+} were adopted based on previous recommendations [30]. The
591 previous m-12-6-4-LJ model was developed to incorporate the polarizabilities of coordinating atoms,
592 which is crucial for accurately capturing the induced dipole effect in MD simulations of ion transport
593 involving metal ions and coordinating atoms [65-67]. This model was also validated for its effectiveness
594 in simulating metal binding at the selectivity filter, highlighting its sensitivity to the polarizability of

coordinating atoms.

Both ZIP13-WT complexes with Zn^{2+} and Fe^{2+} were simulated for 0.5 μs-MD trajectories with 3 replications to observe ion binding stability using AMBER20 package software [68], as a standard protocol [69, 70]. These systems were prepared for 0.5 μs-MD simulations via CHARMM-GUI [71], featuring box dimensions of 99 × 99 × 123 Å, with 131 1,2-dilauroyl-sn-glycero-3-phosphocholine (DLPC) molecules per leaflet, and 27,442 TIP3P water molecules. System neutralization was achieved with a 0.15 M KCl concentration, with an additional 0.05 M ZnCl and FeCl added to ZIP13/Zn^{2+} and ZIP13/Fe^{2+}, respectively. Protein and ions were treated by ff19SB Amber forcefield [72] and 12-6-4 Lennard-Jones model, respectively. Five-step minimization, utilizing steepest descent and conjugate gradient methods with restriction from the protein backbone to the side chain, was conducted for 10,000 steps at each stage. Subsequently, a 36 ns NVT heating phase gradually increased the temperature from 0 to 300 K. Production involved 0.5 μs-MD simulations. These MD trajectories were analyzed to assess ion binding stability by the "hbond" action command implemented in the CPPTRAJ [73] module within the AmberTools 21 package program [74]. This technique resembles traditional hydrogen bond interaction analysis but with the angle cutoff disabled and a distance cutoff set at 3.0 Å. The evaluation of ion binding stability was based on the lifetime and average number of amino acids in contact with the ions.

Statistical analysis

All quantitative data were reported as the mean ± standard error of the mean (SEM). Statistical differences between the two groups were analyzed by the two-tailed unpaired Student's *t*-test. For multiple comparisons, analysis of variance (ANOVA) was performed followed by two-way ANOVA with the Bonferroni's multiple comparison test, or one-way ANOVA with the post-hoc Tukey-Kramer test for comparison among groups, or the post-hoc Dunnett test for comparison of groups with a specific control. A *p*-value of less than 0.05 was considered to indicate a statistically significant difference between groups.

Ethics approval

All animal experiments were performed in accordance with institutional and national guidelines and regulations and RIKEN Regulations for the Animal Experiments. The study protocol was approved by the Institutional Animal Care and Use Committee of Gunma University (study approval no.: #19-025), and of RIKEN Kobe Branch (Approval number: A2001-03). This study was reported in accordance with ARRIVE guidelines.

Acknowledgments

We thank Dr. H. A. Popiel, Dr. I. Yanatori, Professor K. Ishimori, Professor T. Kitamura, Professor Y. Tamura, Professor S. Toyokuni, Professor J. Shirakawa, Professor S. Nagamori, Professor K. Iwai, and Dr. T. Kambe for their helpful suggestions and discussions, and Ms. Y. Miyazaki, Ms. Y. Tamura,

633 Ms. W. Mizutani, and Ms. A. Suda for their technical assistance. We also appreciate the assistance
634 from the Mouse Facility Core of Gunma University. This work was supported by a Grant-in-Aid for
635 Scientific Research on Innovative Areas "Integrated Bio-metal Science" (MEXT KAKENHI grant
636 number JP22H04801 to A.F.), and JP22K8618, and JP19K08971 (to A.F.), 20H03409 (to T.F.) from
637 the Ministry of Education, Culture, Sports, Science, and Technology, Japan; grants from Takeda
638 Science Foundation, The Koyanagi Foundation, The TANITA Healthy Weight Community Trust,
639 Kanae Foundation for the promotion of Medical Science, Front Runner of Future Diabetes Research
640 Foundation, the Shiseido Female Researcher Science Grant, The Cell Science Research Foundation,
641 and The Ichiro Kanehara Foundation (all to A.F.). This work was also supported by research grant
642 from the Secom Science and Technology Foundation (to Y.F.). This work was carried out by the joint
643 research program of the Institute for Molecular and Cellular Regulation, Gunma University (18010
644 to T.F.).

645

646 **Author contributions**

647 A.F. conceived the project. A.F. performed the experiments and analyzed the data. G.T., and T.K.
648 performed the oocyte transport experiments. A.F., and D.S. conducted the metabolic studies. K.H.
649 performed *in silico* study of ion binding site evaluation. T.I., and I.A. performed the ICP-MS and
650 fluorescence-activated cell sorting (FACS) experiments, respectively. M. Shimura, T.S., and Y.N.
651 analyzed the data. M. Shigeta, H.K., and T.F. generated *Zip13*-flox mice. T.H., and I.H. provided the

adiponectin-Cre mice. A.F. wrote the original manuscript, and A.F., H. Shibata, K.H., Y.S., H Sakurai, S.K., H.W., T.F., and Y.F. reviewed the manuscript. T.F., and Y.F. supervised the project.

Declaration of interests

The authors declare no competing interests in association with this study.

658 **Figure legends**

659 **Fig. 1. Adipo-*Zip13*KO mice accelerated lipolysis.** (A) Relative mRNA levels of *Zip13* in the
660 indicated tissues of 34-week-old Ctrl (n = 5) and Adipo-*Zip13*KO mice (n = 4). (B) Relative mRNA
661 expression of *Zip13* in the subcutaneous fat tissue of WT mice (n = 5), fed STD or HFD for 12 weeks
662 from 6-weeks old. (C) Body weights of the indicted mice fed a STD or HFD. Ctrl STD, n = 9 to 23;
663 Adipo-*Zip13*KO STD, n = 7 to 19; Ctrl HFD, n = 17; Adipo-*Zip13*KO HFD, n = 22. (D) Body weight
664 of 34-week-old Ctrl (n = 8) and Adipo-*Zip13*KO mice (n = 9). (E) Tissue weights of subcutaneous,
665 visceral, and brown fat tissues of 34-week-old Ctrl (n = 8) and Adipo-*Zip13*KO (n = 9) mice. (F, G)
666 Whole-body RER of 20-week-old Ctrl (n = 8) and Adipo-*Zip13*KO mice (n = 9) fed a STD. (F): RER
667 trend, (G): RER period. (H) Plasma NEFA levels of 6-weeek old Ctrl (n = 8 to 13) and Adipo-
668 *Zip13*KO mice (n = 9 to 11) fasted overnight and the i.p. injected with isoproterenol. (I) NEFA release
669 from the indicated fat explants treated with saline (Basal) or isoproterenol (Iso). Fold changes are
670 shown as stimulated/basal lipolysis. Analyzed fat pads were from 28 to 32-week old Ctrl (n = 6) and
671 Adipo-*Zip13*KO mice (n = 7). (J) NEFA release from Ctrl and Adipo-*Zip13*KO differentiated cells
672 treated with dimethyl sulfoxide (DMSO) (Basal) and isoproterenol (Iso). Data are shown as the mean
673 ± SEM. (A, B, C, D, E, G, and I) $^{*}p < 0.05$, $^{**}p < 0.01$, by the two-tailed unpaired Student's *t*-test. In
674 (J and H), $^{*}p < 0.05$, by two-way ANOVA followed by the Bonferroni's multiple comparison test. ns,
675 not significant.

676

677 **Fig. 2. Adipo-*Zip13*KO mouse adipocytes increased intracytoplasmic iron levels but decreased**
678 **organelles iron levels.** (A) Zinc and iron levels in mature adipocytes. Zinc and iron level were
679 measured by ICP-MS. (B) Zn^{2+} and Fe^{2+} levels in Ctrl and Adipo-*Zip13*KO mature adipocyte cells.
680 Zn^{2+} and Fe^{2+} levels were detected by using FluoZin-3 and FerroOrange, respectively. (C)
681 Immunofluorescence staining of mZIP13-HA in preadipocytes. Insertion of an HA sequence at C-
682 terminal end allowed immunofluorescence studies using anti-HA antibody. Scale bar 50 μm. GM130:
683 Golgi marker, Calreticulin, ER marker. (D) Immunoblotting of IRP2, TfR, FTL, Fth1, and actin using
684 whole cell extracts of differentiated Ctrl and Adipo-*Zip13*KO cells treated with dimethyl sulfoxide
685 (DMSO) (Basal) or isoproterenol (Iso). Actin was included as a loading control. (E) Each protein
686 shown in (D) was quantified by normalization to actin. Data are shown as the mean ± SEM. In (A, B
687 and E), $^{*}p < 0.05$, $^{**}p < 0.01$, $^{***}p < 0.001$, by the two-tailed unpaired Student's *t*-test.

688

689 **Fig. 3. ZIP13-mediated iron negatively regulates lipolysis.**
690 (A) Schematic representation of the experimental plan. (B) Zn^{2+} and Fe^{2+} level in *Zip13* KO
691 preadipocyte cells expressing ZIP13-WT and ZIP13-H254A. (C) Zn^{2+} and Fe^{2+} levels in *Zip13* KO
692 mature adipocyte cells expressing ZIP13-WT and ZIP13-H254A. (D) NEFA release from Adipo-
693 *Zip13*KO mature adipocyte cells expressing ZIP13-WT or ZIP13-H254A, and treated with DMSO
694 (Basal) and isoproterenol (Iso). (E) Total iron levels of Ctrl and Adipo-*Zip13*KO preadipocyte and
695 mature adipocyte cells. (F) Total zinc levels of Ctrl and Adipo-*Zip13*KO preadipocyte and mature

696 adipocyte cells. (G) Schematic representation of the experimental plan (upper panel). Ctrl and Adipo-
697 *Zip13*KO cells were differentiated by stimulation with isoproterenol, in the presence or absence of N-
698 acetylcysteine (NAC), and then NEFA release was analyzed (lower panel). Data are shown as the
699 mean ± SEM. In (B, C, D, E, and F), *$p < 0.05$, **$p < 0.01$, ***$p < 0.001$, ****$p < 0.0001$, by one-way
700 ANOVA followed by the post-hoc Tukey-Kramer test. In (G), *$p < 0.05$, by the two-tailed unpaired
701 Student's *t*-test. ns, not significant.

702

703 **Fig. 4. PDE activity is reduced in Adipo-*Zip13*KO cells.** (A) Immunoblotting of pPKA, PKA, and
704 GAPDH in subcutaneous fat tissues from Ctrl and Adipo-*Zip13*KO mice, stimulated with DMSO
705 (basal) (left panel) or isoproterenol (Iso) (right panel). (B) cAMP levels of Ctrl and Adipo-*Zip13*KO
706 mature adipocytes in the presence (Iso) or absence (Basal) of isoproterenol. (C) NEFA release from
707 differentiated Ctrl and Adipo-*Zip13*KO mature adipocytes stimulated with isoproterenol, or forskolin.
708 (D) PDE activity in Ctrl and Adipo-*Zip13*KO mature adipocytes, normalized by protein concentration.
709 (E) NEFA release from the differentiated Ctrl and Adipo-*Zip13*KO cells, stimulated with cilostamide
710 (PDE3 inhibitor), or rolipram (PDE4 inhibitor). (F) PDE activity normalized by protein concentration
711 of Ctrl adipocyte cells in the presence or absence of H_2O_2. Data are shown as the mean ± SEM. In (A,
712 D, and F), *$p < 0.05$, ****$p < 0.0001$, by the two-tailed unpaired Student's *t*-test. In (B and C), *$p < 0.05$,
713 ****$p < 0.0001$, by one-way ANOVA followed by the post- hoc Tukey-Kramer test. In (E), **$p < 0.01$,
714 by two-way ANOVA followed by the Bonferroni's multiple comparison test. ns, not significant.

715

716 **Fig. 5. ZIP13 has the ability to transport both zinc and iron.**

717 (A) Immunofluorescence microscopic detection of the expression of mZIP13, hZIP14, 4F2hc-m13,
718 and 4F2hc-m14 in *X. laevis* oocytes. Insertion of an HA sequence at the C-terminal end enabled
719 immunofluorescence analyses using an anti-HA antibody. Scale bar = 50 μm. (B) Schematic
720 illustration of 4F2hc-m13 and 4F2hc-m14. (C) Alphafold2 simulation of the fusion protein of 4F2hc
721 and mZIP13. (D) Relative *MT1* expression in HEK293 cells expressing 4F2hc, 4F2hc-m13, or 4F2hc-
722 m14 with the addition of 20 μM $ZnSO_4$ was added. (E) Zinc uptake of 4F2hc-m13 and 4F2hc-m14.
723 (F) Iron uptake of 4F2hc-m13 and 4F2hc-m14. Data are shown as the mean ± SEM. In (C), $^{*}p < 0.05$,
724 $^{**}p < 0.01$, $^{***}p < 0.001$, $^{****}p < 0.0001$, by one-way ANOVA followed by the post-hoc Tukey-
725 Kramer test. In (E and F), $^{****}p < 0.0001$, by the two-tailed unpaired Student's *t*-test. Ext. extracellular
726 space, Int. intracellular space.

727

728 **Fig. 6. Ion binding site prediction and analysis of mouse ZIP13 protein.**

729 (A) The ion binding site of representative structure of ZIP13 at M1 and M2 embedded in lipid
730 membrane (right panel) and motion of ions and amino acid residues in the M1 and M2 sites, where
731 red to blue color change indicates the time lapse (left panel). (B) The number of atom contacts
732 (#contact) to ion during the 0.5 μs-MD simulations. (C) Occupancy of Zn^{2+}/Fe^{2+} ions nearby amino
733 acid residues at the M1 and M2 sites. Oδ and Oε mean two different oxygens in the carboxy group,

734 and Nε does the Nε atom in the histidine.

735

736 **Fig. 7. ZIP13 regulates adipocyte lipolysis through ZIP13-mediated iron.**

737 Schematic illustration of metal ion balance in preadipocytes and mature adipocytes. Zinc level is
738 slightly decreased during adipocyte differentiation, whereas iron level is dramatically increased
739 during adipocyte differentiation (upper right panel). ZIP13-mediated iron suppresses the β-adrenergic
740 receptor signaling pathway, thereby inhibiting lipolysis.

741

742 **References**

743 1 Auger, C. & Kajimura, S. Adipose Tissue Remodeling in Pathophysiology. *Annu Rev*
744 *Pathol* **18**, 71-93 (2023). https://doi.org/10.1146/annurev-pathol-042220-023633
745 2 Angueira, A. R. *et al.* Defining the lineage of thermogenic perivascular adipose tissue.
746 *Nat Metab* **3**, 469-484 (2021). https://doi.org/10.1038/s42255-021-00380-0
747 3 Tamaki, M. *et al.* The diabetes-susceptible gene SLC30A8/ZnT8 regulates hepatic
748 insulin clearance. *J Clin Invest* **123**, 4513-4524 (2013).
749 https://doi.org/10.1172/JCI68807
750 4 Krishnamoorthy, L. *et al.* Copper regulates cyclic-AMP-dependent lipolysis. *Nat Chem*
751 *Biol* **12**, 586-592 (2016). https://doi.org/10.1038/nchembio.2098
752 5 Joffin, N. *et al.* Adipose tissue macrophages exert systemic metabolic control by
753 manipulating local iron concentrations. *Nat Metab* **4**, 1474-1494 (2022).
754 https://doi.org/10.1038/s42255-022-00664-z
755 6 Misu, H. *et al.* Deficiency of the hepatokine selenoprotein P increases responsiveness
756 to exercise in mice through upregulation of reactive oxygen species and AMP-activated
757 protein kinase in muscle. *Nat Med* **23**, 508-516 (2017). https://doi.org/10.1038/nm.4295
758 7 Jiang, J. *et al.* Thermogenic adipocyte-derived zinc promotes sympathetic innervation
759 in male mice. *Nat Metab* **5**, 481-494 (2023). https://doi.org/10.1038/s42255-023-
760 00751-9
761 8 Fukunaka, A. & Fujitani, Y. Role of Zinc Homeostasis in the Pathogenesis of Diabetes
762 and Obesity. *Int J Mol Sci* **19** (2018). https://doi.org/10.3390/ijms19020476
763 9 Jeong, J. & Eide, D. J. The SLC39 family of zinc transporters. *Mol Aspects Med* **34**,
764 612-619 (2013). https://doi.org/10.1016/j.mam.2012.05.011
765 10 Jenkitkasemwong, S. *et al.* SLC39A14 Is Required for the Development of
766 Hepatocellular Iron Overload in Murine Models of Hereditary Hemochromatosis. *Cell*
767 *Metab* **22**, 138-150 (2015). https://doi.org/10.1016/j.cmet.2015.05.002
768 11 Wang, G. *et al.* Metastatic cancers promote cachexia through ZIP14 upregulation in
769 skeletal muscle. *Nat Med* **24**, 770-781 (2018). https://doi.org/10.1038/s41591-018-
770 0054-2
771 12 Lin, W. *et al.* Hepatic metal ion transporter ZIP8 regulates manganese homeostasis and
772 manganese-dependent enzyme activity. *J Clin Invest* **127**, 2407-2417 (2017).
773 https://doi.org/10.1172/JCI90896

774 13 Park, J. H. *et al.* SLC39A8 Deficiency: A Disorder of Manganese Transport and
775 Glycosylation. *Am J Hum Genet* **97**, 894-903 (2015).
776 https://doi.org/10.1016/j.ajhg.2015.11.003
777 14 Scheiber, I. F., Wu, Y., Morgan, S. E. & Zhao, N. The intestinal metal transporter ZIP14
778 maintains systemic manganese homeostasis. *J Biol Chem* **294**, 9147-9160 (2019).
779 https://doi.org/10.1074/jbc.RA119.008762
780 15 Jeong, J. *et al.* Promotion of vesicular zinc efflux by ZIP13 and its implications for
781 spondylocheiro dysplastic Ehlers-Danlos syndrome. *Proc Natl Acad Sci U S A* **109**,
782 E3530-3538 (2012). https://doi.org/10.1073/pnas.1211775110
783 16 Bin, B. H. *et al.* Biochemical characterization of human ZIP13 protein: a homo-
784 dimerized zinc transporter involved in the spondylocheiro dysplastic Ehlers-Danlos
785 syndrome. *J Biol Chem* **286**, 40255-40265 (2011).
786 https://doi.org/10.1074/jbc.M111.256784
787 17 Bin, B. H. *et al.* Molecular pathogenesis of spondylocheirodysplastic Ehlers-Danlos
788 syndrome caused by mutant ZIP13 proteins. *EMBO Mol Med* **6**, 1028-1042 (2014).
789 https://doi.org/10.15252/emmm.201303809
790 18 Fukunaka, A. *et al.* Zinc transporter ZIP13 suppresses beige adipocyte biogenesis and
791 energy expenditure by regulating C/EBP-beta expression. *PLoS Genet* **13**, e1006950
792 (2017). https://doi.org/10.1371/journal.pgen.1006950
793 19 Speliotes, E. K. *et al.* Association analyses of 249,796 individuals reveal 18 new loci
794 associated with body mass index. *Nat Genet* **42**, 937-948 (2010).
795 https://doi.org/10.1038/ng.686
796 20 Willer, C. J. *et al.* Discovery and refinement of loci associated with lipid levels. *Nat*
797 *Genet* **45**, 1274-1283 (2013). https://doi.org/10.1038/ng.2797
798 21 Fukada, T. *et al.* The zinc transporter SLC39A13/ZIP13 is required for connective tissue
799 development; its involvement in BMP/TGF-beta signaling pathways. *PLoS One* **3**,
800 e3642 (2008). https://doi.org/10.1371/journal.pone.0003642
801 22 Giunta, C. *et al.* Spondylocheiro dysplastic form of the Ehlers-Danlos syndrome--an
802 autosomal-recessive entity caused by mutations in the zinc transporter gene SLC39A13.
803 *Am J Hum Genet* **82**, 1290-1305 (2008). https://doi.org/10.1016/j.ajhg.2008.05.001
804 23 Xiao, G., Wan, Z., Fan, Q., Tang, X. & Zhou, B. The metal transporter ZIP13 supplies
805 iron into the secretory pathway in Drosophila melanogaster. *Elife* **3**, e03191 (2014).

806 https://doi.org/10.7554/eLife.03191
807 24 Hirayama T, et al. A highly selective turn-on fluorescent probe for iron (II) to visualize
808 labile iron in living cells. *Chemical Science* **3**, (2013).
809 https://doi.org/10.1039/C2SC21649C
810 25 Zhang, T. *et al.* Crystal structures of a ZIP zinc transporter reveal a binuclear metal
811 center in the transport pathway. *Sci Adv* **3**, e1700344 (2017).
812 https://doi.org/10.1126/sciadv.1700344
813 26 Rumberger, J. M., Peters, T., Jr., Burrington, C. & Green, A. Transferrin and iron
814 contribute to the lipolytic effect of serum in isolated adipocytes. *Diabetes* **53**, 2535-
815 2541 (2004). https://doi.org/10.2337/diabetes.53.10.2535
816 27 Grabner, G. F., Xie, H., Schweiger, M. & Zechner, R. Lipolysis: cellular mechanisms
817 for lipid mobilization from fat stores. *Nat Metab* **3**, 1445-1465 (2021).
818 https://doi.org/10.1038/s42255-021-00493-6
819 28 Snyder, P. B., Esselstyn, J. M., Loughney, K., Wolda, S. L. & Florio, V. A. The role of
820 cyclic nucleotide phosphodiesterases in the regulation of adipocyte lipolysis. *J Lipid*
821 *Res* **46**, 494-503 (2005). https://doi.org/10.1194/jlr.M400362-JLR200
822 29 Makino, H., de Buschiazzo, P. M., Pointer, R. H., Jordan, J. E. & Kono, T.
823 Characterization of insulin-sensitive phosphodiesterase in fat cells. I. Effects of salts
824 and oxidation-reduction agents. *J Biol Chem* **255**, 7845-7849 (1980).
825 30 Jiang, Y. *et al.* Rational engineering of an elevator-type metal transporter ZIP8 reveals
826 a conditional selectivity filter critically involved in determining substrate specificity.
827 *Commun Biol* **6**, 778 (2023). https://doi.org/10.1038/s42003-023-05146-w
828 31 Harrison, A. V., Lorenzo, F. R. & McClain, D. A. Iron and the Pathophysiology of
829 Diabetes. *Annu Rev Physiol* **85**, 339-362 (2023). https://doi.org/10.1146/annurev-
830 physiol-022522-102832
831 32 Iwasaki, T. *et al.* Serum ferritin is associated with visceral fat area and subcutaneous fat
832 area. *Diabetes Care* **28**, 2486-2491 (2005). https://doi.org/10.2337/diacare.28.10.2486
833 33 Cepeda-Lopez, A. C. *et al.* Sharply higher rates of iron deficiency in obese Mexican
834 women and children are predicted by obesity-related inflammation rather than by
835 differences in dietary iron intake. *Am J Clin Nutr* **93**, 975-983 (2011).
836 https://doi.org/10.3945/ajcn.110.005439
837 34 Pinhas-Hamiel, O. *et al.* Greater prevalence of iron deficiency in overweight and obese

838 children and adolescents. *Int J Obes Relat Metab Disord* **27**, 416-418 (2003).
839 https://doi.org/10.1038/sj.ijo.0802224
840 35 Cohen, P. & Kajimura, S. The cellular and functional complexity of thermogenic fat.
841 *Nat Rev Mol Cell Biol* **22**, 393-409 (2021). https://doi.org/10.1038/s41580-021-00350-
842 0
843 36 Sakers, A., De Siqueira, M. K., Seale, P. & Villanueva, C. J. Adipose-tissue plasticity
844 in health and disease. *Cell* **185**, 419-446 (2022).
845 https://doi.org/10.1016/j.cell.2021.12.016
846 37 Long, J. Z. *et al.* A smooth muscle-like origin for beige adipocytes. *Cell Metab* **19**, 810-
847 820 (2014). https://doi.org/10.1016/j.cmet.2014.03.025
848 38 Oguri, Y. *et al.* CD81 Controls Beige Fat Progenitor Cell Growth and Energy Balance
849 via FAK Signaling. *Cell* **182**, 563-577 e520 (2020).
850 https://doi.org/10.1016/j.cell.2020.06.021
851 39 Abe, I. *et al.* Lipolysis-derived linoleic acid drives beige fat progenitor cell proliferation.
852 *Dev Cell* **57**, 2623-2637 e2628 (2022). https://doi.org/10.1016/j.devcel.2022.11.007
853 40 Xu, J., Wan, Z. & Zhou, B. Drosophila ZIP13 is posttranslationally regulated by iron-
854 mediated stabilization. *Biochim Biophys Acta Mol Cell Res* **1866**, 1487-1497 (2019).
855 https://doi.org/10.1016/j.bbamcr.2019.06.009
856 41 Zhao, M. & Zhou, B. A distinctive sequence motif in the fourth transmembrane domain
857 confers ZIP13 iron function in Drosophila melanogaster. *Biochim Biophys Acta Mol*
858 *Cell Res* **1867**, 118607 (2020). https://doi.org/10.1016/j.bbamcr.2019.118607
859 42 Joffin, N. *et al.* Mitochondrial metabolism is a key regulator of the fibro-inflammatory
860 and adipogenic stromal subpopulations in white adipose tissue. *Cell Stem Cell* **28**, 702-
861 717 e708 (2021). https://doi.org/10.1016/j.stem.2021.01.002
862 43 Moreno-Navarrete, J. M., Ortega, F., Moreno, M., Ricart, W. & Fernandez-Real, J. M.
863 Fine-tuned iron availability is essential to achieve optimal adipocyte differentiation and
864 mitochondrial biogenesis. *Diabetologia* **57**, 1957-1967 (2014).
865 https://doi.org/10.1007/s00125-014-3298-5
866 44 Pang, C., Chai, J., Zhu, P., Shanklin, J. & Liu, Q. Structural mechanism of intracellular
867 autoregulation of zinc uptake in ZIP transporters. *Nat Commun* **14**, 3404 (2023).
868 https://doi.org/10.1038/s41467-023-39010-6
869 45 Zhang, Y. *et al.* Structural insights into the elevator-type transport mechanism of a

870 bacterial ZIP metal transporter. *Nat Commun* **14**, 385 (2023).
871 https://doi.org/10.1038/s41467-023-36048-4
872 46 Wiuf, A. *et al.* The two-domain elevator-type mechanism of zinc-transporting ZIP
873 proteins. *Sci Adv* **8**, eabn4331 (2022). https://doi.org/10.1126/sciadv.abn4331
874 47 Gaither, L. A. & Eide, D. J. Functional expression of the human hZIP2 zinc transporter.
875 *J Biol Chem* **275**, 5560-5564 (2000). https://doi.org/10.1074/jbc.275.8.5560
876 48 Hoch, E., Levy, M., Hershfinkel, M. & Sekler, I. Elucidating the H(+) Coupled Zn(2+)
877 Transport Mechanism of ZIP4; Implications in Acrodermatitis Enteropathica. *Int J Mol*
878 *Sci* **21** (2020). https://doi.org/10.3390/ijms21030734
879 49 Shigihara, N. *et al.* Human IAPP-induced pancreatic beta cell toxicity and its regulation
880 by autophagy. *J Clin Invest* **124**, 3634-3644 (2014). https://doi.org/10.1172/JCI69866
881 50 Yagi, T. *et al.* A novel ES cell line, TT2, with high germline-differentiating potency.
882 *Anal Biochem* **214**, 70-76 (1993). https://doi.org/10.1006/abio.1993.1458
883 51 Hausman, D. B., Park, H. J. & Hausman, G. J. Isolation and culture of preadipocytes
884 from rodent white adipose tissue. *Methods Mol Biol* **456**, 201-219 (2008).
885 https://doi.org/10.1007/978-1-59745-245-8_15
886 52 Fukunaka, A. *et al.* Tissue nonspecific alkaline phosphatase is activated via a two-step
887 mechanism by zinc transport complexes in the early secretory pathway. *J Biol Chem*
888 **286**, 16363-16373 (2011). https://doi.org/10.1074/jbc.M111.227173
889 53 Fukunaka, A. *et al.* Demonstration and characterization of the heterodimerization of
890 ZnT5 and ZnT6 in the early secretory pathway. *J Biol Chem* **284**, 30798-30806 (2009).
891 https://doi.org/10.1074/jbc.M109.026435
892 54 Fukunaka, A. *et al.* Zinc and iron dynamics in human islet amyloid polypeptide-induced
893 diabetes mouse model. *Sci Rep* **13**, 3484 (2023). https://doi.org/10.1038/s41598-023-
894 30498-y
895 55 Kanai, Y. *et al.* Expression cloning and characterization of a transporter for large neutral
896 amino acids activated by the heavy chain of 4F2 antigen (CD98). *J Biol Chem* **273**,
897 23629-23632 (1998). https://doi.org/10.1074/jbc.273.37.23629
898 56 Hojyo, S. *et al.* The zinc transporter SLC39A14/ZIP14 controls G-protein coupled
899 receptor-mediated signaling required for systemic growth. *PLoS One* **6**, e18059 (2011).
900 https://doi.org/10.1371/journal.pone.0018059
901 57 Schweiger, M. *et al.* Measurement of lipolysis. *Methods Enzymol* **538**, 171-193 (2014).

https://doi.org/10.1016/B978-0-12-800280-3.00010-4

58 Hirayama, T. Fluorescent probes for the detection of catalytic Fe(II) ion. *Free Radic Biol Med* **133**, 38-45 (2019). https://doi.org/10.1016/j.freeradbiomed.2018.07.004

59 Jutabha, P. *et al.* Human sodium phosphate transporter 4 (hNPT4/SLC17A3) as a common renal secretory pathway for drugs and urate. *J Biol Chem* **285**, 35123-35132 (2010). https://doi.org/10.1074/jbc.M110.121301

60 Mirdita, M. *et al.* ColabFold: making protein folding accessible to all. *Nat Methods* **19**, 679-682 (2022). https://doi.org/10.1038/s41592-022-01488-1

61 David Sehnal, et al. Mol* Viewer: modern web app for 3D visualization and analysis of large biomolecular structures. *Nucleic Acids Res*. **49**, W431–W437 (2021). https://doi.org/10.1093/nar/gkab314

62 Shimura, M. *et al.* Imaging of intracellular fatty acids by scanning X-ray fluorescence microscopy. *FASEB J* 30, 4149-4158 (2016). http://doi.org/1o.1096/fj.201600569R

63 Jumper, J. *et al.* Highly accurate protein structure prediction with AlphaFold. *Nature* **596**, 583-589 (2021). https://doi.org/10.1038/s41586-021-03819-2

64 Ireland, S. M. & Martin, A. C. R. ZincBind-the database of zinc binding sites. *Database (Oxford)* **2019** (2019). https://doi.org/10.1093/database/baz006

65 Parise, A. & Magistrato, A. Assessing the mechanism of fast-cycling cancer-associated mutations of Rac1 small Rho GTPase. *Protein Sci* **33**, e4939 (2024). https://doi.org/10.1002/pro.4939

66 Puyo-Fourtine, *et al.* Consistent Picture of Phosphate–Divalent Cation Binding from Models with Implicit and Explicit Electronic Polarization. *The Journal of Physical Chemistry B* **126**, 4022-4034 (2022). https://doi.org/10.1021/acs.jpcb.2c01158

67 Mels, O. *et al.* Benchmarking biomolecular force field-based Zn2+ for mono- and bimetallic ligand binding sites. *Journal of Computational Chemistry* **44**, 912-926 (2023). https://doi.org/10.1002/jcc.27052

68 D.A. Case, K. B., I.Y. Ben-Shalom, S.R. Brozell, D.S. Cerutti, T.E. Cheatham, III, V.W.D. Cruzeiro, T.A. Darden, R.E. Duke, G. Giambasu, M.K. Gilson, H. Gohlke, A.W. Goetz, R. Harris, S. Izadi, S.A. Izmailov, K. Kasavajhala, A. Kovalenko, R. Krasny, T. Kurtzman, T.S. Lee, S. LeGrand, P. Li, C. Lin, J. Liu, T. Luchko, R. Luo, V. Man, K.M. Merz, Y. Miao, O. Mikhailovskii, G. Monard, H. Nguyen, A. Onufriev, F.Pan, S. Pantano, R. Qi, D.R. Roe, A. Roitberg, C. Sagui, S. Schott-Verdugo, J. Shen, C.L. Simmerling, N.R.Skrynnikov, J. Smith, J. Swails, R.C. Walker, J. Wang, L. Wilson,

R.M. Wolf, X. Wu, Y. Xiong, Y. Xue, D.M. York and P.A. Kollman. *AMBER 2020*. (2020).

69 Hengphasatporn, K. *et al.* Promising SARS-CoV-2 main protease inhibitor ligand-binding modes evaluated using LB-PaCS-MD/FMO. *Scientific Reports* **12**, 17984 (2022). https://doi.org/10.1038/s41598-022-22703-1

70 Hengphasatporn, K. *et al.* Halogenated Baicalein as a Promising Antiviral Agent toward SARS-CoV-2 Main Protease. *Journal of Chemical Information and Modeling* **62**, 1498-1509 (2022). https://doi.org/10.1021/acs.jcim.1c01304

71 Jo, S., Kim, T., Iyer, V. G. & Im, W. CHARMM-GUI: a web-based graphical user interface for CHARMM. *J Comput Chem* **29**, 1859-1865 (2008). https://doi.org/10.1002/jcc.20945

72 Tian, C. *et al.* ff19SB: Amino-Acid-Specific Protein Backbone Parameters Trained against Quantum Mechanics Energy Surfaces in Solution. *J Chem Theory Comput* **16**, 528-552 (2020). https://doi.org/10.1021/acs.jctc.9b00591

73 Roe, D. R. & Cheatham, T. E., 3rd. PTRAJ and CPPTRAJ: Software for Processing and Analysis of Molecular Dynamics Trajectory Data. *J Chem Theory Comput* **9**, 3084-3095 (2013). https://doi.org/10.1021/ct400341p

74 Case, D. *et al.* AmberTools21. *University of California: San Francisco, CA, USA* (2021).

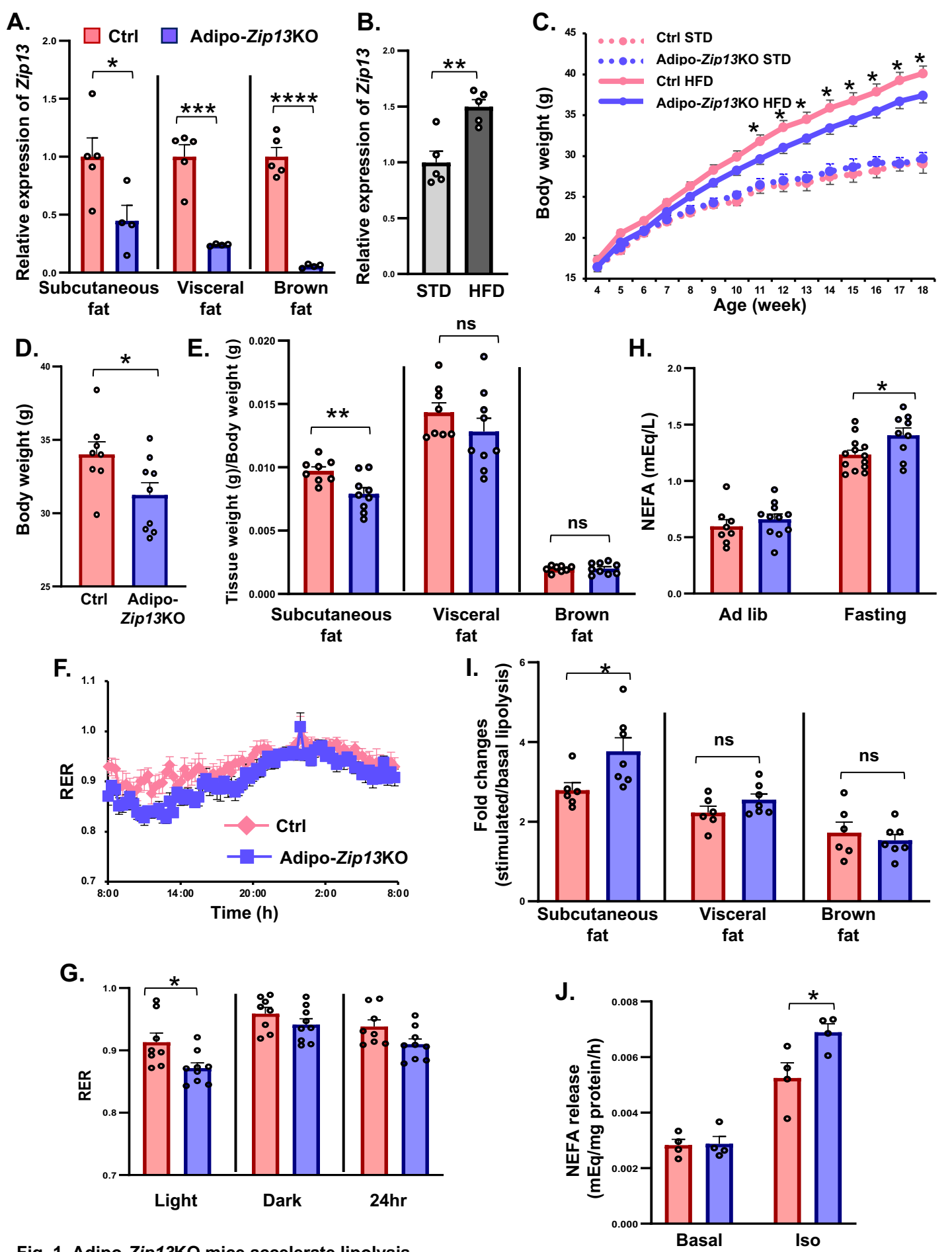

Fig. 1. Adipo-*Zip13*KO mice accelerate lipolysis.

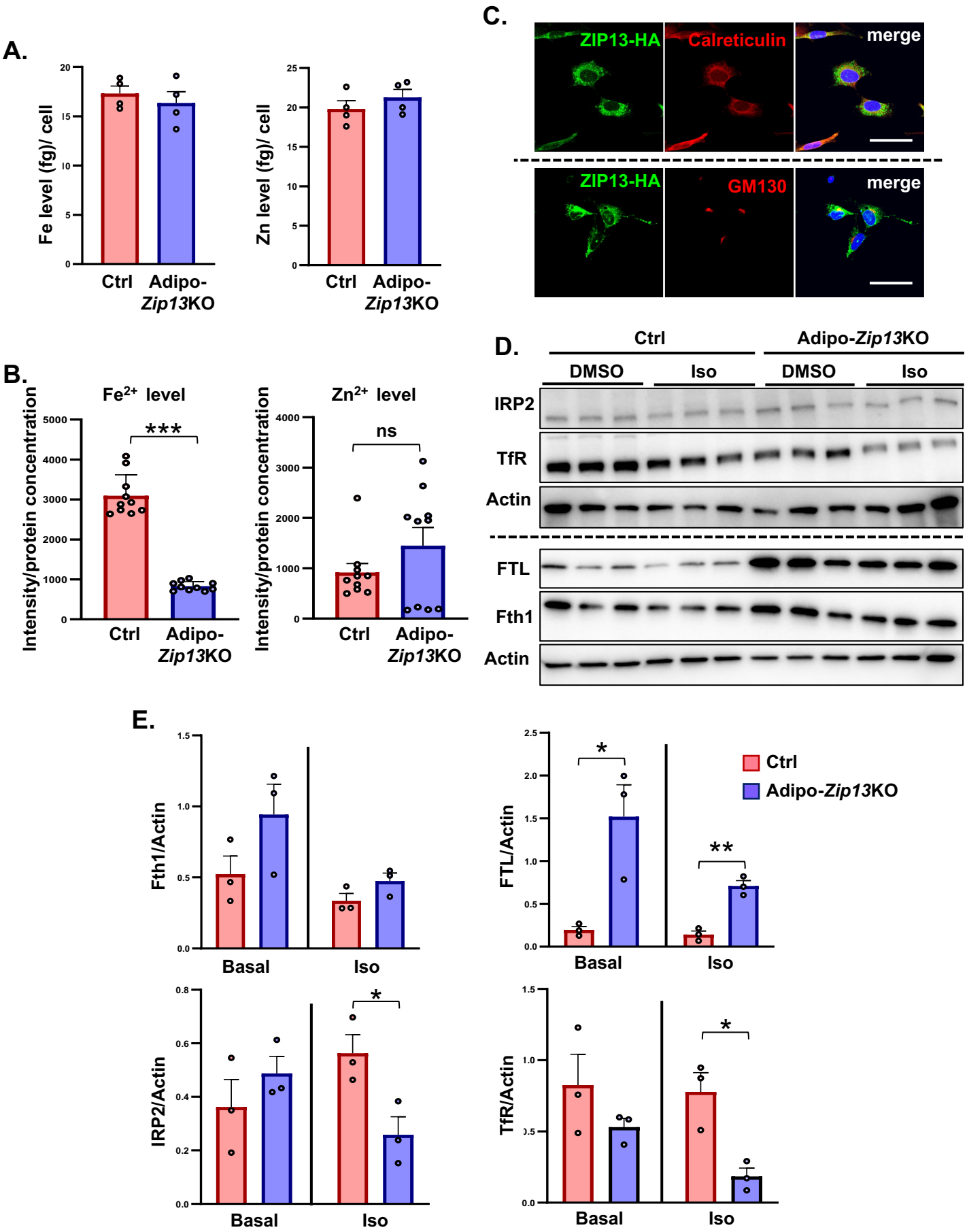

Fig. 2. Adipo-*Zip13*KO mouse adipocytes increased intracytoplasmic iron levels but decreased organelles iron level.

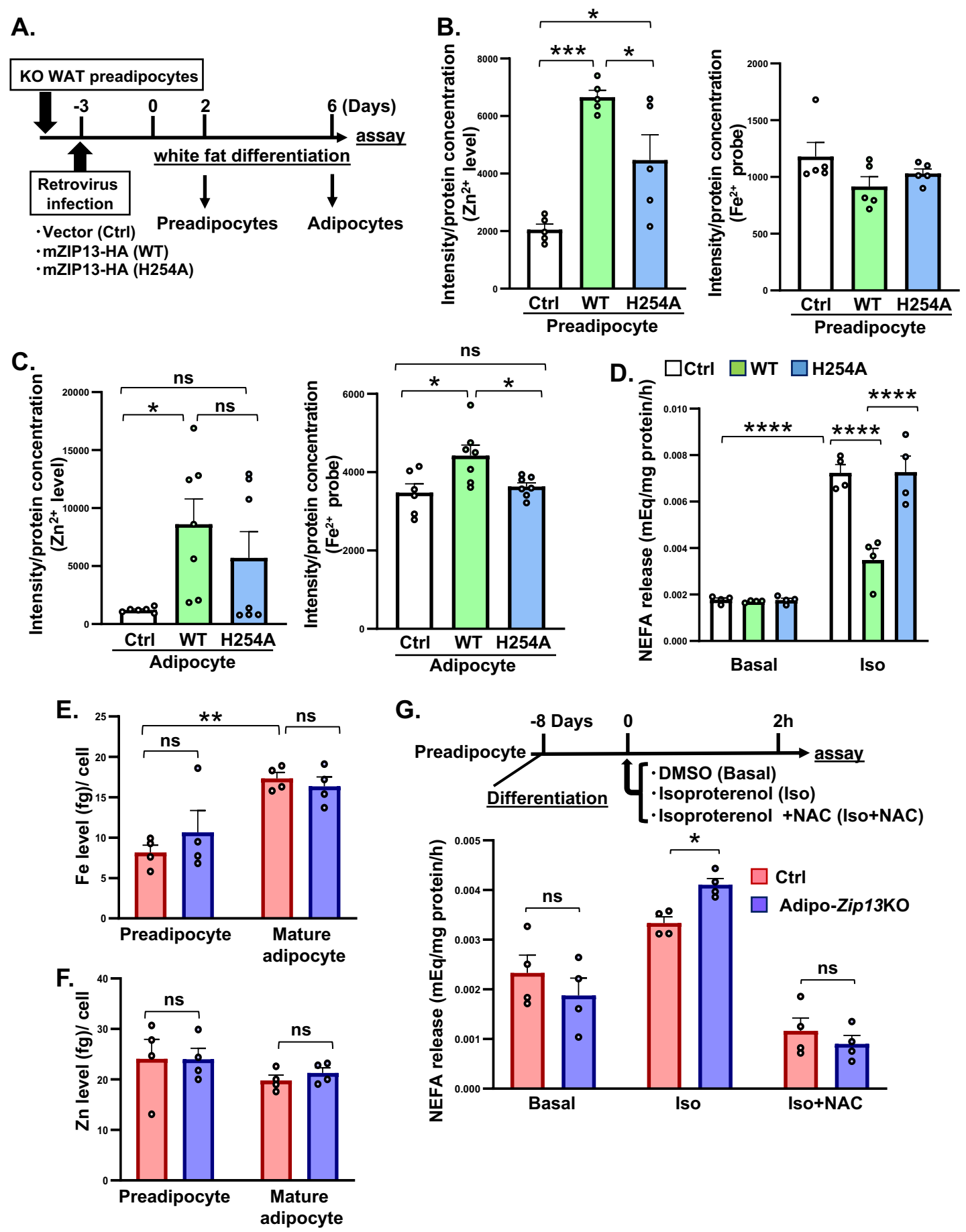

Fig. 3. ZIP13-mediated iron negatively regulates lipolysis.

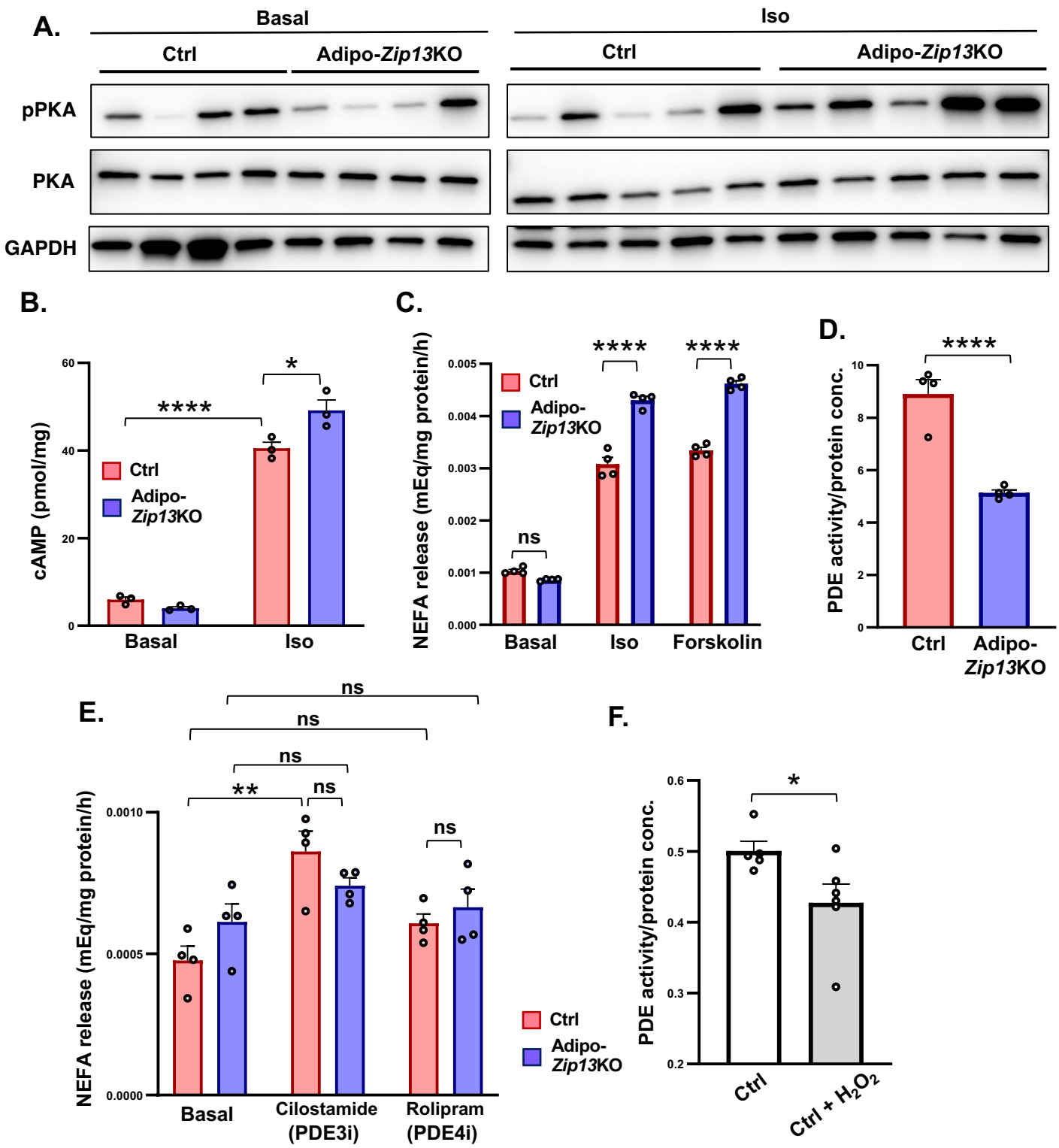

Fig. 4. PDE activity is reduced in Adipo-*Zip13*KO cells.

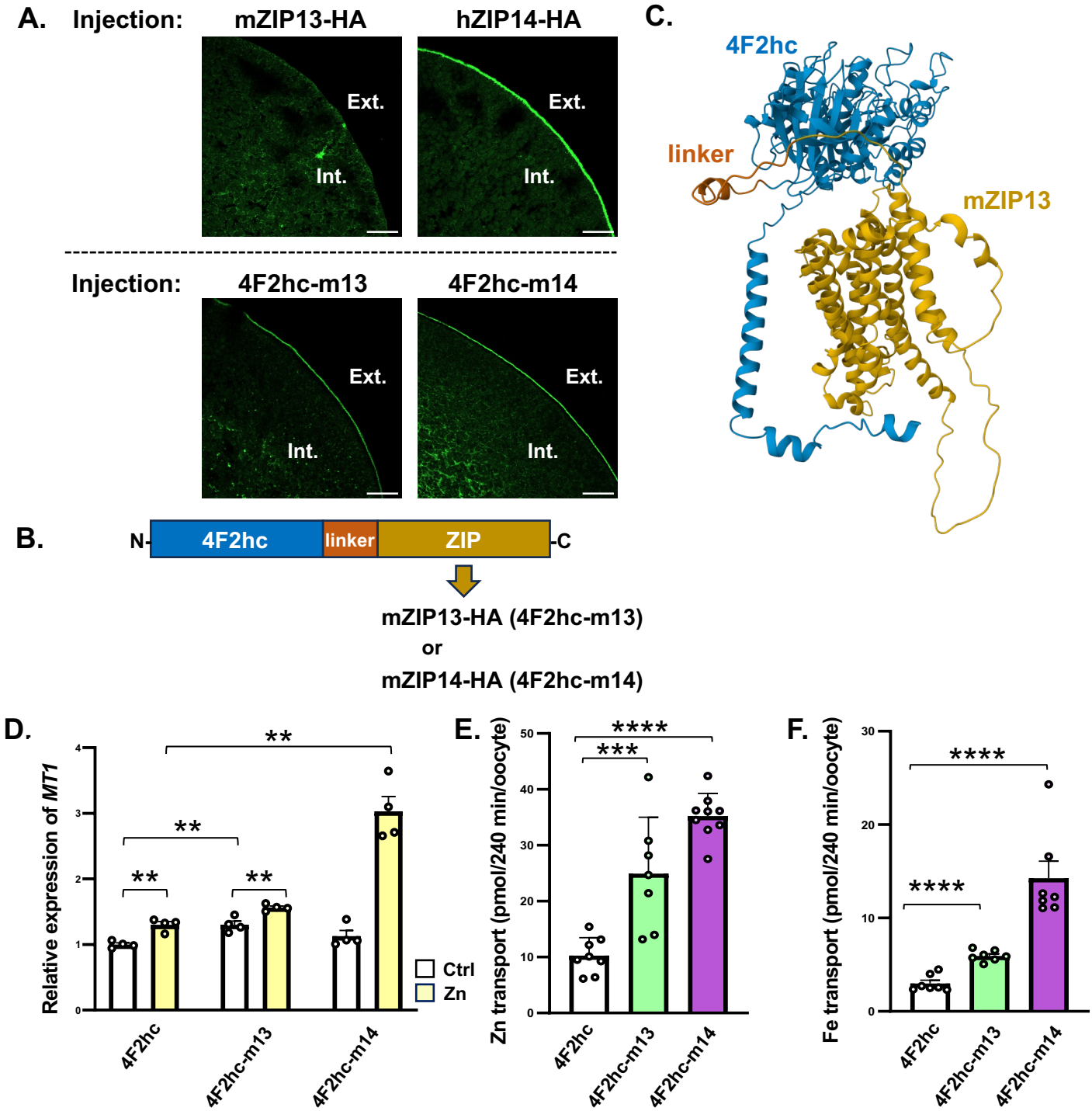

Fig. 5. ZIP13 has the ability to transport both zinc and iron.

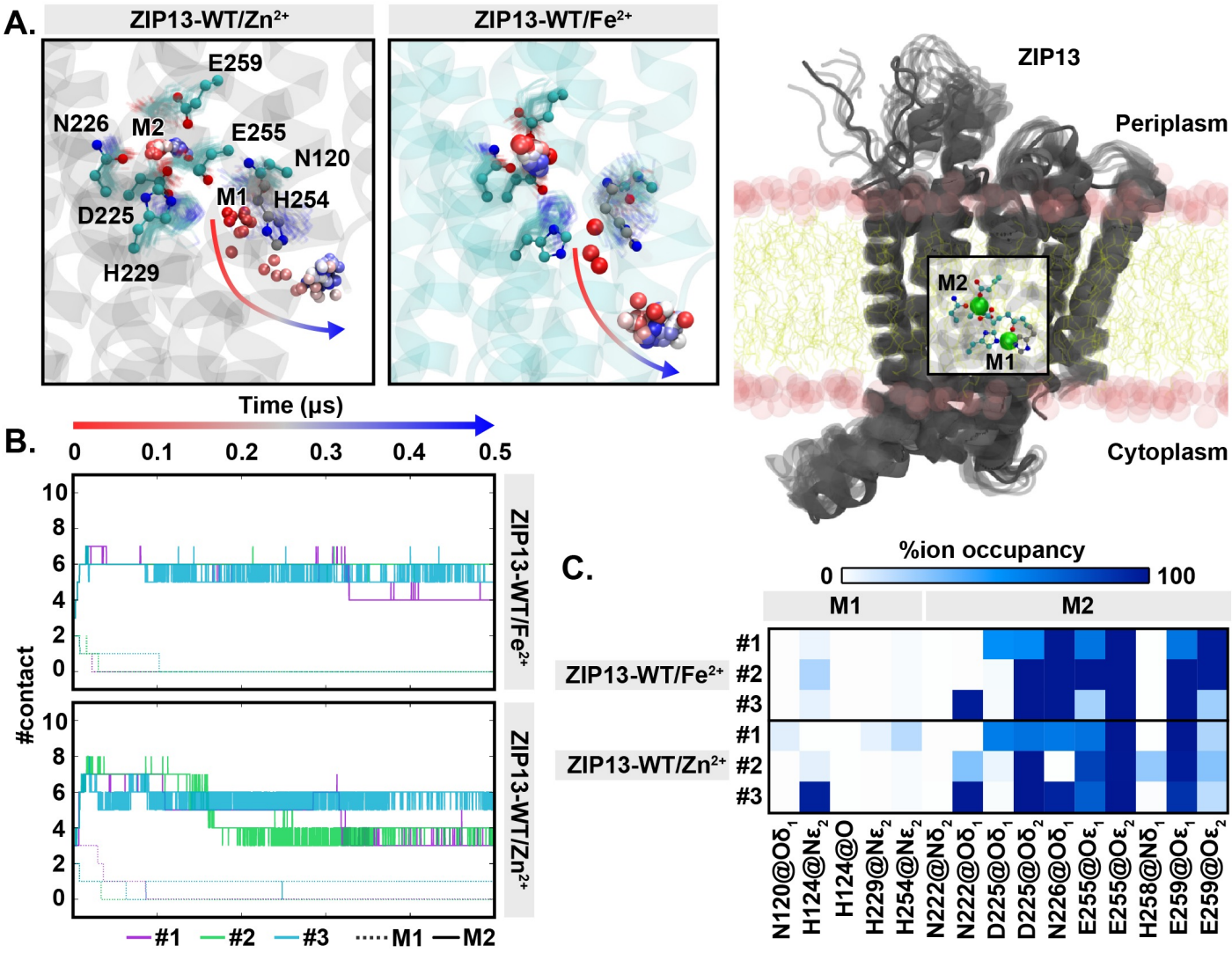

Fig. 6. Ion binding site prediction and analysis of mouse ZIP13 protein.

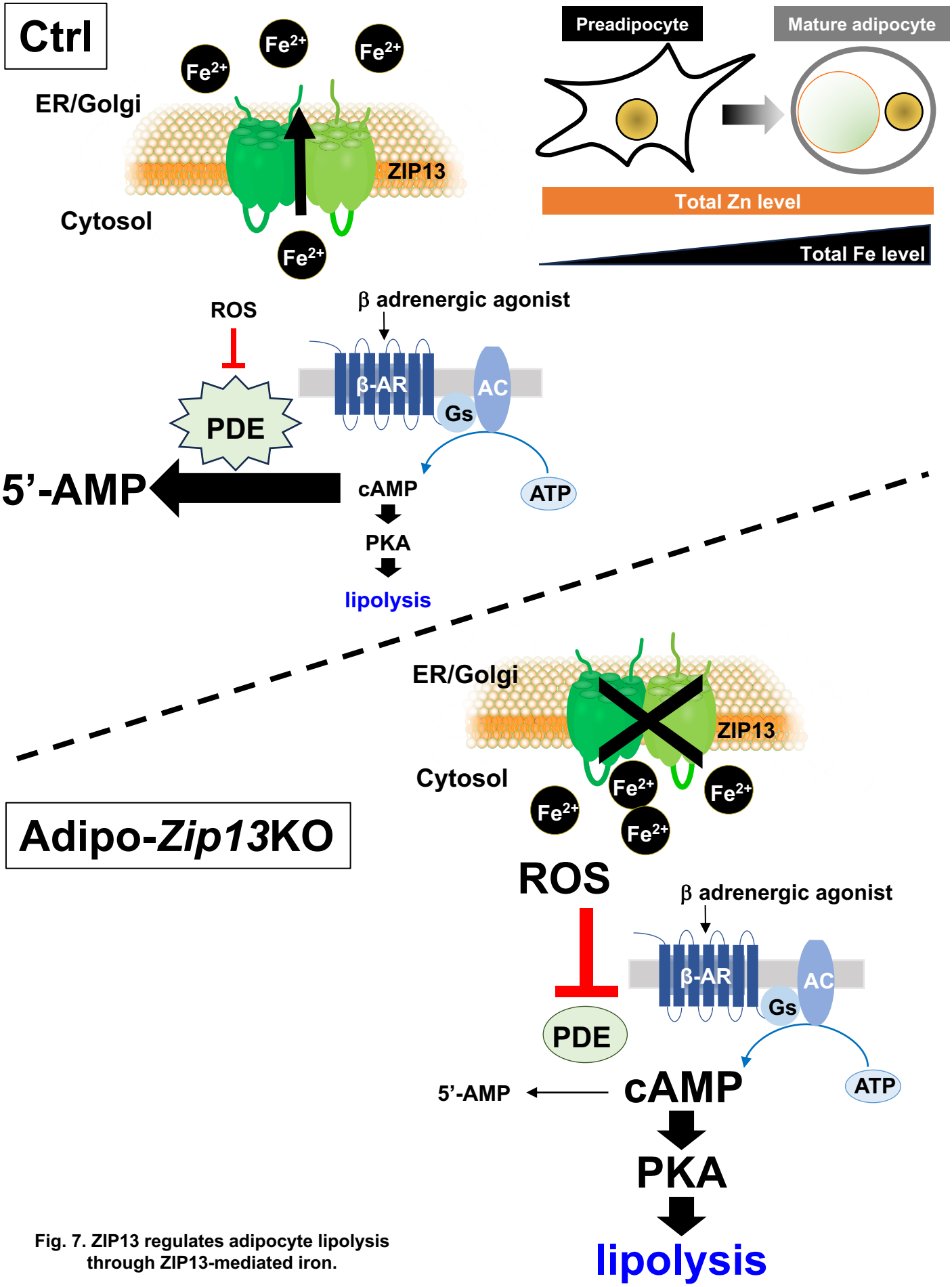

Fig. 7. ZIP13 regulates adipocyte lipolysis through ZIP13-mediated iron.